Università degli Studi di Roma Tor Vergata

DIPARTIMENTO DI INGEGNERIA ELETTRONICA

Master di II Livello in "Ingegneria e diritto internazionale dello spazio nei sistemi di comunicazione, navigazione e sensing satellitare"

Hyperspectral unmixing based on Artificial Intelligence and optimization methods applied to ASI's PRISMA data

Relatore Prof.ssa Ernestina CIANCA

Co-relatore

Dr. Matteo PICCHIANI (ASI)

Candidato
Vincenzo GIORDANO – 0353409

Acknowledgements

I wish to express my most sincere gratitude first and foremost to the Italian Navy General Staff for granting me the invaluable opportunity to delve into the Earth Observation topics that most captured my interest during this Master's program.

A special and profound thank you is owed to my co-supervisor, Dr. Matteo Picchiani of the Italian Space Agency (ASI). His support throughout this research was not only constant and invaluable, even when provided remotely, but also exceptional in both its technical depth and its human dimension. I am particularly grateful for the remarkable flexibility he demonstrated in accommodating my highly dynamic schedule as a Navy Officer, skillfully balancing his own demanding work commitments with my research activities. His guidance, patience, and understanding were instrumental to the successful completion of this thesis.

Sommario

L'imaging iperspettrale (Hyperspectral Imaging - HSI) è diventato uno strumento inestimabile nell'osservazione della Terra, fornendo ricche informazioni spettrali attraverso centinaia di bande strette e contigue. Questa capacità consente una caratterizzazione e identificazione dettagliata dei materiali sulla superficie terrestre. Tuttavia, la risoluzione spaziale dei sensori HSI satellitari, come PRISMA (PRecursore IperSpettrale della Missione Applicativa) dell'Agenzia Spaziale Italiana (ASI), porta spesso ad avere pixel che contengono una miscela di materiali diversi (pixel misti). Le tecniche di decomposizione spettrale (spectral unmixing) mirano ad affrontare questa sfida scomponendo lo spettro misurato di un pixel misto in una collezione di spettri puri costituenti (endmember) e le loro corrispondenti abbondanze frazionali. Un accurato spectral unmixing è cruciale per numerose applicazioni, tra cui il monitoraggio ambientale, l'agricoltura di precisione, l'esplorazione mineraria e la gestione dei disastri.

Questa tesi presenta lo sviluppo e la valutazione di una metodologia ibrida di spectral unmixing progettata per i dati iperspettrali PRISMA, integrando approcci geometrico/statistici tradizionali con tecniche di intelligenza artificiale. L'obiettivo primario era creare un flusso di lavoro robusto ed efficiente, capace di identificare accuratamente gli endmember e stimare le loro abbondanze da scene iperspettrali complesse.

La metodologia proposta inizia con il pre-processamento dei dati PRISMA, che include la concatenazione delle bande VNIR e SWIR e l'associazione con le lunghezze d'onda corrispondenti. Un aspetto chiave dell'approccio è una robusta strategia di inizializzazione degli endmember che impiega molteplici algoritmi consolidati: Vertex Component Analysis (VCA), Principal Component Analysis (PCA) e N-FINDR. Questi metodi sfruttano diverse proprietà geometriche e statistiche dei dati iperspettrali per identificare potenziali endmember candidati. Gli endmember inizializzati servono come input per una Rete Neurale Convoluzionale (Convolutional Neural Network - CNN), che viene addestrata per affinare le firme spettrali degli endmember apprendendo complesse caratteristiche spettro-spaziali da sottoinsiemi di dati. Questa componente di deep learning mira a migliorare l'accuratezza e la discriminabilità degli endmember finali. A seguito dell'affinamento basato sulla CNN, le abbondanze frazionali per ciascun endmember all'interno di ogni pixel vengono stimate utilizzando l'algoritmo dei minimi quadrati non negativi (non-negative least squares -Isqnonneg), garantendo l'aderenza ai vincoli fisici (non negatività e somma unitaria implicitamente gestite attraverso il processo). Infine, una fase sperimentale prevede il tentativo di associare le firme spettrali degli endmember estratti con materiali noti, confrontandoli con la libreria spettrale del Jet Propulsion Laboratory (JPL) della NASA

utilizzando le metriche Spectral Angle Mapper (SAM) e Spectral Information Divergence (SID).

L'efficacia della pipeline proposta è stata dimostrata utilizzando un dataset iperspettrale PRISMA. I risultati mostrano l'estrazione riuscita di firme spettrali di endmember distinti e la generazione delle corrispondenti mappe di abbondanza che rivelano pattern spaziali significativi correlati alle caratteristiche del suolo. L'analisi di cross-correlazione ha confermato l'unicità degli endmember identificati. Per valutare ulteriormente la robustezza e la generalizzabilità del nucleo di unmixing (inizializzazione + CNN), il modello è stato testato anche sul dataset iperspettrale ampiamente utilizzato dell'Università di Pavia, acquisito dal sensore ROSIS. Nonostante le differenze nelle caratteristiche del sensore e la mancanza di informazioni specifiche sulla lunghezza d'onda per Pavia, il modello ha separato con successo le principali classi di copertura del suolo presenti nella scena, allineandosi bene con le informazioni di ground truth e dimostrando l'adattabilità dell'approccio.

Sebbene il processo centrale di unmixing abbia prodotto risultati promettenti, l'associazione finale con la libreria spettrale JPL tramite SAM e SID ha evidenziato difficoltà nel raggiungere un'elevata confidenza e accuratezza. Questo passaggio rimane un'area che richiede ulteriori indagini, potenzialmente coinvolgendo metriche di similarità più sofisticate, strategie di filtraggio della libreria o tecniche di confronto basate sulle caratteristiche spettrali (feature-based matching).

In conclusione, questa tesi contribuisce a definire un nuovo framework ibrido per lo spectral unmixing che sinergizza i punti di forza dei metodi di inizializzazione tradizionali e del deep learning (CNN) per migliorare l'estrazione degli endmember dai dati PRISMA. Il metodo dimostra robustezza ed efficienza, in particolare lavorando con sottoinsiemi di dati. Il lavoro futuro dovrebbe concentrarsi sul miglioramento dell'affidabilità dell'associazione automatica tra gli endmember estratti e le librerie spettrali di riferimento, al fine di massimizzare l'applicabilità pratica dei risultati dell'unmixing per compiti quantitativi di telerilevamento.

Abstract

Hyperspectral imaging (HSI) has become an invaluable tool in Earth observation, providing rich spectral information across hundreds of narrow, contiguous bands. This capability allows for detailed characterization and identification of materials on the Earth's surface. However, the spatial resolution of satellite-based HSI sensors, such as the Italian Space Agency's (ASI) PRISMA (PRecursore IperSpettrale della Missione Applicativa), often leads to pixels containing a mixture of different materials (mixed pixels). Spectral unmixing techniques aim to address this challenge by decomposing the measured spectrum of a mixed pixel into a collection of constituent pure spectra (endmembers) and their corresponding fractional abundances. Accurate spectral unmixing is crucial for numerous applications, including environmental monitoring, precision agriculture, mineral exploration, and disaster management.

This thesis presents the development and evaluation of a hybrid spectral unmixing methodology designed for PRISMA hyperspectral data, integrating traditional geometric/statistical approaches with artificial intelligence techniques. The primary objective was to create a robust and efficient workflow capable of accurately identifying endmembers and estimating their abundances from complex hyperspectral scenes.

The proposed methodology begins with preprocessing of the PRISMA data, involving the concatenation of VNIR and SWIR bands and association with corresponding wavelengths. A key aspect of the approach is a robust endmember initialization strategy employing multiple established algorithms: Vertex Component Analysis (VCA), Principal Component Analysis (PCA), and N-FINDR. These methods leverage different geometric and statistical properties of the hyperspectral data to identify potential endmember candidates. The initialized endmembers serve as input for a Convolutional Neural Network (CNN), which is trained to refine the endmember signatures by learning complex spectral-spatial features from data subsets. This deep learning component aims to improve the accuracy and discriminability of the final endmembers. Following the CNN-based refinement, the fractional abundances for each endmember within each pixel are estimated using the nonnegative least squares (Isqnonneg) algorithm, ensuring adherence to physical constraints (non-negativity and sum-to-one implicitly managed through the process). Finally, an experimental step involves attempting to associate the extracted endmember signatures with known materials by comparing them against the NASA Jet Propulsion Laboratory (JPL) spectral library using the Spectral Angle Mapper (SAM) and Spectral Information Divergence (SID) metrics.

The effectiveness of the proposed pipeline was demonstrated using a PRISMA hyperspectral dataset. Results show the successful extraction of distinct endmember signatures and the

generation of corresponding abundance maps that reveal meaningful spatial patterns related to ground features. Cross-correlation analysis confirmed the uniqueness of the identified endmembers. To further assess the robustness and generalizability of the unmixing core (initialization + CNN), the model was also tested on the widely used Pavia University hyperspectral dataset, acquired by the ROSIS sensor. Despite differences in sensor characteristics and the lack of specific wavelength information for Pavia, the model successfully separated the main land cover classes present in the scene, aligning well with ground truth information and demonstrating the adaptability of the approach.

While the core unmixing process yielded promising results, the final association with the JPL spectral library using SAM and SID highlighted challenges in achieving high confidence and accuracy. This step remains an area requiring further investigation, potentially involving more sophisticated similarity metrics, library filtering strategies, or feature-based matching techniques.

To conclude, this thesis introduces a novel hybrid framework for spectral unmixing. By synergizing the strengths of traditional initialization methods and deep learning (specifically CNNs), this framework offers potentially improved endmember extraction from PRISMA data. The method demonstrates robustness and efficiency, particularly when working with data subsets. Future work should focus on enhancing the reliability of the automatic association between extracted endmembers and reference spectral libraries to maximize the practical applicability of the unmixing results for quantitative remote sensing tasks.

Table of Contents

| Acknowledgements | I |
|--|-----|
| Sommario | III |
| Abstract | V |
| Table of Contents | VII |
| List of Figures | IX |
| List of Tables | XI |
| 1.1 Solar Radiation and Electromagnetic Spectrum | 1 |
| 1.2 Interaction between electromagnetic waves and matter | |
| 1.3 Interaction of Solar Radiation with the Atmosphere | |
| 1.3.1 Atmospheric Absorption | |
| 1.3.2 Atmospheric Scattering | 3 |
| 1.4 Definitions | |
| 1.4.1 Radiance | 4 |
| 1.4.2 Spectral Radiance | 4 |
| 1.4.3 Spectral Emissivity | 5 |
| 2.1 Origins of Hyperspectral Imaging | 7 |
| 2.2 Current Applications | 8 |
| 2.2.1 Environmental Monitoring | 8 |
| 2.2.2 Agriculture | 9 |
| 2.2.3 Mineral Exploration | 9 |
| 2.2.4 Disaster Management: | 9 |
| 2.2.5 Urban Planning and Infrastructure: | 9 |
| 3.1 The Mission | 11 |
| 3.2 Space segment | 12 |
| 3.2.1 Payload | 13 |
| 3.3 Ground segment | 15 |
| 3.4 PRISMA Product | 16 |
| 3.5 Orbit and coverage | 17 |
| 4.1 Introduction to Hyperspectral Unmixing | 19 |
| 4.2 Linear vs. Nonlinear Spectral Unmixing | 19 |
| 4.3 Unsupervised Endmember Extraction | |
| 4.3.1 Principal Component Analysis (PCA) | 20 |
| 4.3.2 Vertex Component Analysis (VCA) | |
| 4.3.3 Pixel Purity Index (PPI): | 22 |
| 4.3.4 N-FINDR | 23 |
| 4.4 Supervised Endmember Extraction | 23 |

| 4.5 | Advanced Spectral Unmixing Techniques | 24 |
|----------|--|----|
| 4.5. | | |
| 4.5.2 | | |
| 5.1 | Data Preprocessing | 27 |
| 5.2 | Band-Wavelength Association | 28 |
| 5.3 | Hyperspectral Unmixing | 28 |
| 5.3. | | |
| 5.3.2 | 2 CNN for Endmember Extraction | 29 |
| 5.3.3 | Abundance Estimation using Isqnonneg | 29 |
| 5.4 | Spectral Library Import | 30 |
| 5.5 | Endmember Comparison | 31 |
| 6.1 | Identified Endmembers | 33 |
| 6.2 | Abundances | 36 |
| 6.3 | Model validation | 42 |
| 6.4 | Association with existing library | 46 |
| 7.1 | Summary and Contributions | |
| 7.2 | Advantages of the Proposed Method | 50 |
| 7.3 | Challenges and Future Directions for Library Association | 50 |
| 7.4 | Concluding Remarks | 51 |
| Acronyr | ns | 53 |
| Bibliogr | aphy | 57 |

List of Figures

| Figure 1-1 The Electromagnetic Spetrum | 2 |
|---|-------|
| Figure 1-2. Atmospheric Absorbtion | 3 |
| Figure 2-1. Example of Hyperspectral mission application – ESA Copernicus | 8 |
| Figure 3-1. Pushbroom scanning concept for recording reflected radiation from the Earth surface | ce.12 |
| Figure 3-2. PRISMA Satellite | 13 |
| Figure 3-3. The PRISMA sensor. | 14 |
| Figure 3-4. ASI's PRISMA Mission Area of interest | 18 |
| Figure 6-1. Spectral signatures – Endmembers 1 to 4 | 33 |
| Figure 6-2. Spectral signatures – Endmembers 5 to 8 | 34 |
| Figure 6-3. Spectral signatures – Endmembers 9 to 12 | 34 |
| Figure 6-4. Endmembers' spectra cross-correlations. | 35 |
| Figure 6-5. Abundance map – Endmember 1 | 36 |
| Figure 6-6. Abundance map – Endmember 2 | 36 |
| Figure 6-7. Abundance map – Endmember 3 | 37 |
| Figure 6-8. Abundance map – Endmember 4 | 37 |
| Figure 6-9. Abundance map – Endmember 5 | 38 |
| Figure 6-10. Abundance map – Endmember 6 | 38 |
| Figure 6-11. Abundance map – Endmember 7 | 39 |
| Figure 6-12. Abundance map – Endmember 8 | 39 |
| Figure 6-13. Abundance map – Endmember 9 | 40 |
| Figure 6-14. Abundance map – Endmember 10 | 40 |
| Figure 6-15. Abundance map – Endmember 11 | 41 |
| Figure 6-16 Abundance map – Endmember 12 | 41 |
| Figure 6-17. University of Pavia – Pancromatic (left) vs Hyperspectral classes (right) | 42 |
| Figure 6-18. Endmembers extracted by the proposed model from University of Pavia Data | 43 |
| Figure 6-19. Endmember cross-correlation (University of Pavia Dataset) | 43 |
| Figure 6-20. Abundances maps (Endmembers 1 to 4) | 44 |
| Figure 6-21. Abundances maps (Endmembers 5 to 8) | 44 |
| Figure 6-22. Abundances maps (Endmembers 9 to 12) | 45 |

List of Tables

| Table 3-1. Main characteristics of the PRISMA payload | 13 |
|---|------------|
| Table 3-2. PRISMA orbit parameters | 17 |
| Table 6-1. Groundtruth classes for the Pavia University scene and their respective samp | les number |
| | 42 |

Chapter 1 Remote Sensing of Earth

Since the beginning of last century, when the humankind was able to fly and observe the Earth from high altitudes, it was clear that the novel point of view could provide extremely useful information for better understanding the world we live in. Aereal photography provided the first means to quickly assess what was happening on ground, including natural phenomena, troups movements and civilian and military facility usage. Additionally, with the introduction of more sophisticated technologies, aereal photography became an extremely useful tool for broader uses, such as 3D mapping of landscapes (using stereoscopic imaging techniques), environmental and vegetation alanysis (using the first color films) up to the introduction of digital sensors, when it became possible to detect and analyse also different bands of the electromagnetic spectrum. With the "Space Age", when mankind was able to launch satellites in Earth orbit, the possibilities increased dramatically. At the same time, however, technical and physical challenges increased as well, requiring to address new problems.

1.1 Solar Radiation and Electromagnetic Spectrum

Before going more in detail about remote sensing, it is important to mention the physics that stands behind it, in order to better understand what is the added value of using multiple bands fo the solar radiation. Our star, the Sun, constantly emits energy in the form of Electromagnetic radiation (EMR) across a wide range of wavelengths, collectively known as the "electromagnetic spectrum". Part of this spectrum can be directly observed with our eyes, specifically with the retina, while the greates part of it is outside the visible spectrum. Depending on the wavelength (λ), the spectrum can be divided as follows:

- 1. Gamma Rays: $\lambda < 0.01$ nanometers (nm)
- 2. X-rays: $0.01 < \lambda < 10 \text{ nm}$
- 3. Ultraviolet (UV): $10 < \lambda < 400 \text{ nm}$
- 4. Visible Light: $400 < \lambda < 700 \text{ nm}$
- 5. Infrared (IR): 700 nm $< \lambda < 1$ mm
 - a. Near-infrared (NIR): 700 nm $< \lambda < 1.4 \mu m$

b. Mid-infrared: 1.4 μ m < λ < 3 μ m. Used in thermal imaging.

c. Far-infrared: $3 \mu m < \lambda < 1000 \mu m$

6. Microwaves: $\lambda = 1$ mm to 1 m

7. Radio Waves: $\lambda = 1$ m and longer

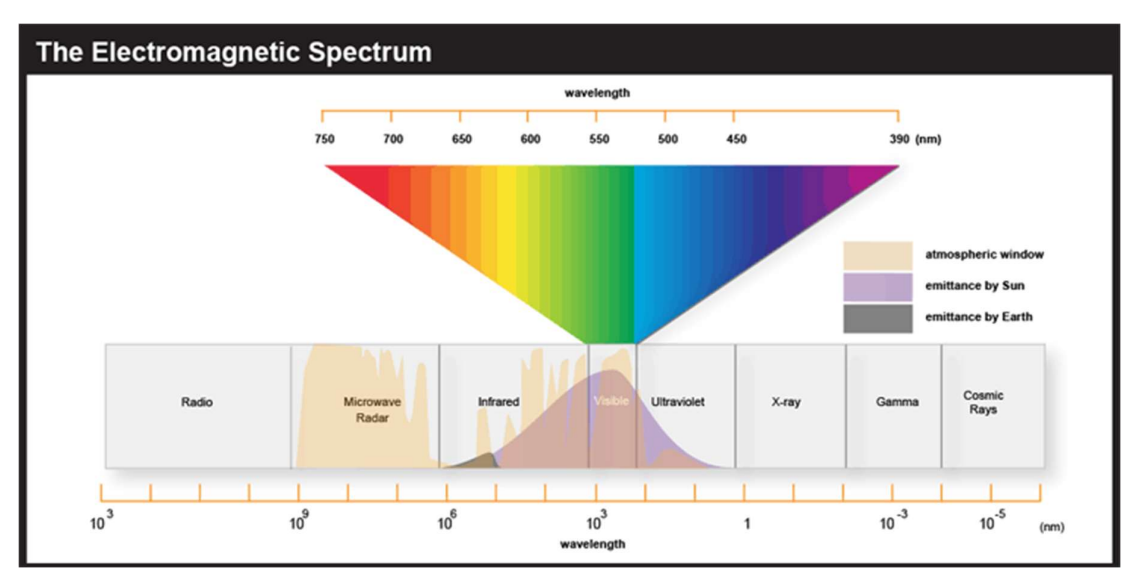


Figure 1-1 The Electromagnetic Spetrum

Each of these bands interacts differently with matter and the atmosphere, providing unique information.

1.2 Interaction between electromagnetic waves and matter

There are few basic ways electromagnetic (EM) waves interacts with matter: reflection, diffraction, refraction, absorption and emission. Now let us describe each in some detail.

- Reflection: it occurs when EM waves bounce off a smooth surface (like mirrors). The angle of incidence is equal to the angle of reflection.
- Diffuse reflection occurs on rough surfaces scattering the EM waves in all directions.
- Diffraction: it is defined as the bending of EM waves around obstacles or through apertures, dependent on wavelength and obstacle size (e.g. light going through small openings or around sharp edges will diffract).
- Refraction: it is defined as the bending of EM waves around obstacles or through apertures when it passes from one medium to another of different optical density causing it to bend.
- Absorption: Absorption occurs when matter absorbs waves energy, often transferring it to heat. Darker objects absorb more visible light than light ones.

- Emission: Any object releases some type of electromagnetic radiation the depends on a temperature. Visual objects such as a star also radiates and gives off both visible and infra-red radiation.
- Scattering: The redirection of light by particles smaller than its wavelength, is responsible for phenomena like the blue color of the sky.

1.3 Interaction of Solar Radiation with the Atmosphere

In order to properly understand what part of the EM spectrum might be used for remote sensing, it is important to describe how the Earth's atmosphere influences the transmission of solar radiation. Key processes include absorption, scattering, and emission.

1.3.1 Atmospheric Absorption

The atmosphere absorbs specific wavelengths of solar radiation due to the presence of gases such as oxygen (O₂), ozone (O₃), carbon dioxide (CO₂), and water vapor (H₂O). These gases create absorption bands, which are regions of the spectrum where radiation is absorbed and does not reach the Earth's surface. More specifically, Water Vapor and CO₂ absorb significant amounts of IR radiation, influencing thermal remote sensing.

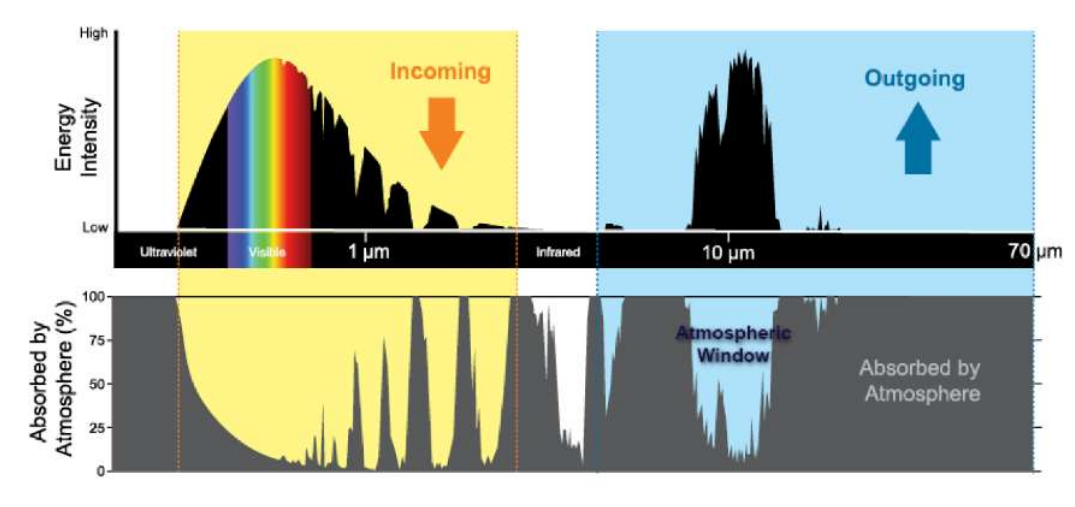


Figure 1-2. Atmospheric Absorbtion

1.3.2 Atmospheric Scattering

As mentioned earlier, scattering affects the path of solar radiation as it passes through the atmosphere. It can reduce the clarity of remote sensing images by introducing haze.

1.4 Definitions

1.4.1 Radiance

Radiance is a measure of the radiant flux emitted, reflected, transmitted, or received by a surface per unit solid angle and per unit projected area. It quantifies how much light travels in a specific direction from a surface. The SI unit of radiance is watts per steradian per square meter $(W \cdot sr^{-1} \cdot m^{-2})$. Radiance is useful for characterizing diffuse emission and reflection of electromagnetic radiation. It indicates how bright an object appears from different angles.

1.4.2 Spectral Radiance

Radiation emitted by a surface can be quantitatively characterized by the concept of spectral radiance, denoted as $I(\lambda, \theta, \varphi, T)$. Spectral radiance represents the power density per unit wavelength and per unit solid angle that traverses a unit surface area oriented orthogonally to the considered direction.

Mathematically, spectral radiance is defined as:

$$I(\lambda, \theta, \varphi, T) = \frac{dW(\lambda, \theta, \varphi,)}{dA \cdot \cos \theta \cdot d\Omega \cdot d\lambda} \left(\frac{W}{m^2 \cdot sr \cdot \mu m} \right)$$
(1.1)

- $dW(\lambda, \theta, \varphi, T)$ is the infinitesimal power radiated by the surface at temperature T through a differential surface element dA,
- dA is the infinitesimal surface area,
- θ and φ are the angles defining the direction of radiation,
- $d\Omega$ is the infinitesimal solid angle centered around the given direction,
- $d\lambda$ is the infinitesimal wavelength interval,
- The cosine term $\cos \theta$ accounts for the projection of the surface element in the considered direction.

This definition encapsulates how radiative energy is distributed as a function of wavelength and direction, making spectral radiance a fundamental quantity in radiative transfer, remote sensing, and thermal emission analysis. For fixed values of λ, θ, ϕ, T the spectral radiance depends solely on the intrinsic physical properties of the emitting object.

1.4.3 Spectral Emissivity

Spectral emissivity is a dimensionless quantity that measures how efficiently an object emits radiation at specific wavelengths compared to an ideal blackbody at the same temperature. It varies between 0 (no emission) and 1 (perfect emission like a blackbody). This concept is crucial for understanding thermal radiation properties.

If the thermodynamic temperature of a surface is known, the measurement of its spectral radiance allows for the determination of its spectral emissivity, $e_{\lambda}(\lambda, \theta, \phi)$. It is defined as:

$$e_{\lambda}(\lambda, \theta, \varphi) = \frac{I(\lambda, \theta, \varphi, T)}{B(\lambda, T)}$$
 (1.2)

where:

- $I(\lambda, \theta, \phi, T)$ is the spectral radiance of the surface at temperature T,
- $B(\lambda, T)$ is the spectral radiance of a black body at the same temperature, given by Planck's law.

The spectral emissivity provides crucial information about the material properties of a surface, influencing applications in thermal imaging, remote sensing, and energy balance studies. A perfect black body has $e_{\lambda} = 1$, while real materials exhibit values lower than unity, depending on wavelength and surface characteristics.

Chapter 2 Hyperspectral Imaging

Hyperspectral imaging (HSI) is a powerful remote sensing technology that has revolutionized the way we observe and analyze the Earth's surface. Unlike traditional imaging techniques that capture data in a few broad spectral bands, hyperspectral imaging collects information across hundreds of narrow, contiguous bands, providing a detailed spectral signature for each pixel in an image. This capability allows for the precise identification and characterization of materials, making hyperspectral imaging an invaluable tool for a wide range of applications, from environmental monitoring to agriculture, mineral exploration, and disaster management.

2.1 Origins of Hyperspectral Imaging

The concept of hyperspectral imaging has its roots in the early 20th century, with the development of spectroscopy and the understanding of the electromagnetic spectrum. Spectroscopy, the study of the interaction between matter and electromagnetic radiation, provided the foundational knowledge necessary for the development of hyperspectral imaging. Early spectroscopic techniques were limited to laboratory settings, where scientists could analyze the spectral properties of materials in controlled environments.

The advent of remote sensing in the mid-twentieth century marked a significant milestone in the evolution of hyperspectral imaging. Remote sensing involves the acquisition of information about an object or phenomenon without making physical contact, typically using sensors mounted on aircraft or satellites. The first remote sensing missions focused on multispectral imaging, which captures data in a few broad spectral bands. While multispectral imaging provided valuable information, it lacked the spectral resolution needed for detailed material identification.

The development of hyperspectral imaging began in the 1980s, driven by advances in sensor technology, computing power, and data processing algorithms. One of the pioneering hyperspectral imaging systems was the Airborne Visible/Infrared Imaging Spectrometer (AVIRIS), developed by NASA's Jet Propulsion Laboratory (JPL) in the late 1980s. AVIRIS

was capable of capturing data in 224 contiguous spectral bands, providing unprecedented spectral resolution for Earth observation.

The success of AVIRIS and other early hyperspectral imaging systems paved the way for the development of spaceborne hyperspectral sensors. The launch of the Hyperion sensor on NASA's EO-1 satellite in 2000 marked a significant milestone in the history of hyperspectral imaging. Hyperion was the first spaceborne hyperspectral sensor capable of capturing data in 220 spectral bands, demonstrating the potential of hyperspectral imaging for global Earth observation.

2.2 Current Applications

Hyperspectral imaging has found applications in a wide range of fields, leveraging its ability to provide detailed spectral information for each pixel in an image. Some of the key applications include:



Figure 2-1. Example of Hyperspectral mission application – ESA Copernicus

2.2.1 Environmental Monitoring

Hyperspectral imaging is widely used for monitoring and managing natural resources and ecosystems. It can detect changes in vegetation health, water quality, and soil composition, making it an invaluable tool for environmental assessment and conservation. For example, hyperspectral data can be used to monitor deforestation, track the spread of invasive species, and assess the impact of climate change on ecosystems.

2.2.2 Agriculture

In agriculture, hyperspectral imaging is used for precision farming, crop health monitoring, and yield prediction. By analyzing the spectral signatures of crops, farmers can detect nutrient deficiencies, water stress, and disease outbreaks, allowing for targeted interventions that optimize resource use and improve crop yields. Hyperspectral imaging also supports the development of sustainable agricultural practices by reducing the need for chemical inputs and minimizing environmental impact.

2.2.3 Mineral Exploration

Hyperspectral imaging is a powerful tool for mineral exploration, enabling the identification of specific minerals based on their unique spectral signatures. This capability is particularly valuable in remote and inaccessible regions, where traditional exploration methods may be impractical. Hyperspectral data can be used to map mineral deposits, assess the potential for resource extraction, and guide exploration efforts.

2.2.4 Disaster Management

Hyperspectral imaging plays a critical role in disaster management, providing timely and accurate information for response and recovery efforts. In the aftermath of natural disasters such as earthquakes, floods, and wildfires, hyperspectral data can be used to assess damage, identify areas at risk, and guide emergency response efforts. For example, hyperspectral imaging can detect changes in land surface temperature, helping to identify hotspots and monitor the spread of wildfires.

2.2.5 Urban Planning and Infrastructure

Hyperspectral imaging is increasingly being used in urban planning and infrastructure development. It can provide detailed information on land use, vegetation cover, and building materials, supporting the development of sustainable and resilient cities. Hyperspectral data can also be used to monitor the condition of infrastructure, such as roads, bridges, and pipelines, enabling proactive maintenance and reducing the risk of failure.

Chapter 3 ASI's PRISMA Satellite

The Italian Space Agency (ASI) has developed and launched a cutting-edge Earth observation satellite named PRISMA (PRecursore IperSpettrale del Sistema di Monitoraggio Ambientale). PRISMA represents a significant leap forward in hyperspectral imaging capabilities, providing crucial data for a wide range of applications, from environmental monitoring and disaster management to agriculture and security. This document outlines the PRISMA mission, its technical characteristics, and its potential impact.

3.1 The Mission

The PRISMA conceptual developments are the result of the HyPSEO project followed by a collaboration between ASI and the Canadian Space Agency for a Phase-A study called JHM. PRISMA has been launched on 22 March 2019 on board the VEGA rocket. PRISMA is a scientific and demonstrative mission. It will play a significant role in the upcoming international scenario of Earth Observation, both for scientific community and for end users, thanks to the capability to acquire worldwide lot of data with a very high spectral resolution and in a wide range of spectral wavelengths. PRISMA provides the capability to acquire, downlink and archive images of all Hyperspectral/Panchromatic channels totaling 200,000 km² daily almost on the entire worldwide area, acquiring square earth tiles of 30km by 30km. The combined hyperspectral and panchromatic products enable the capabilities of recognition of the geometric characteristics of a scene and may provide detailed information about the chemical composition of materials and objects on the Earth surface, giving enormous impacts to remote sensing applications. The PRISMA system includes Ground and Space segments. The PRISMA mission can operate in two modes, a primary mode and a secondary mode. The primary mode of operation is the collection of hyperspectral and panchromatic data from specific individual targets requested by end users. In the secondary mode of operation, the mission will have an established ongoing 'background' task that will acquire imagery to fill up the entire system resources availability.

3.2 Space segment

The PRISMA space segment consists in a single small class spacecraft. The PRISMA payload is a hyperspectral/panchromatic camera with VNIR and SWIR detectors. It consists of an Imaging Spectrometer, able to acquire in a continuum of spectral bands ranging from 400 to 2505 nm (from 400nm to 700nm in VNIR and from 920nm to 2505nm in SWIR) with 30m of spatial resolution and a medium resolution Panchromatic Camera (PAN, from 400nm to 700 nm) with 5m resolution. The PRISMA Hyperspectral sensor utilizes the prism to obtain the dispersion of incoming radiation on a 2-D matrix detectors in order to acquire several spectral bands of the same ground strip. The "instantaneous" spectral and spatial dimensions (across track) of the spectral cube are given directly by the 2-D detectors, while the "temporal" dimension (along track) is given by the satellite motion (pushbroom scanning concept).

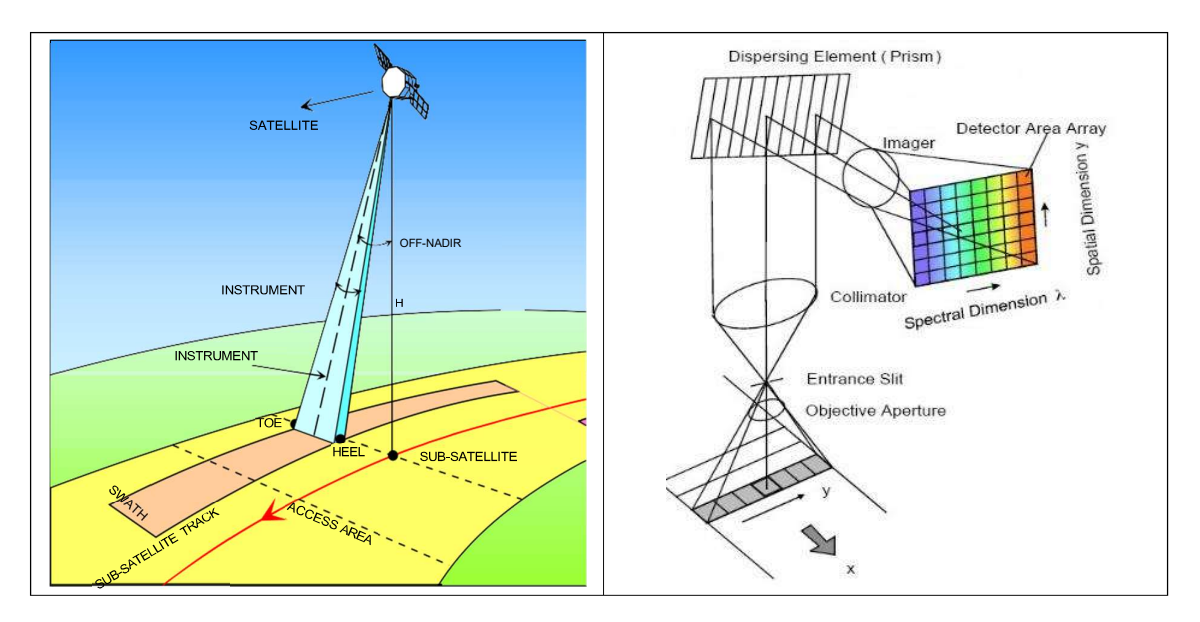


Figure 3-1. Pushbroom scanning concept for recording reflected radiation from the Earth surface.

3.2.1 Payload

The PRISMA Hyperspectral Payload, designed and developed by Leonardo, is a state-of-the-art Electro-Optical instrument composed of a hyperspectral imager optically integrated with a medium resolution panchromatic camera.



Figure 3-2. PRISMA Satellite

| Table 3-1 | Main | characteristics | of the | PRISMA | navload |
|------------|------|-----------------|--------|----------|---------|
| Table 3-1. | wani | CHAIACICHISHICS | or me | LINISIMA | Davidau |

| Swath | 30 Km |
|-------------------|----------------------------------|
| GSD | Hyperspectral: 30 m / PAN: 5 m |
| | VNIR: 400 – 1010 nm |
| | (66 spectral bands) |
| Spectral | SWIR: 920 – 2505 nm |
| Range | (174 spectral bands) |
| | PAN: 400 – 700 nm |
| | VNIR: > 160:1 (>450:1 at 650nm) |
| | SWIR: > 100:1 (>360:1 at 1550nm) |
| SNR | PAN: > 240:1 |
| Spectral Width | ≤ 14.5 nm |

The Payload architecture is composed of the two main subsystems:

- The Hyperspectral / Panchromatic Optical Head (OH)
- The Main Electronics (ME)

The optical design is based on high transmittance optical assemblies, including a reflective common telescope in Three-Mirror Anastigmat (TMA) configuration, a panchromatic camera (700-900 nm), and two spectrometers operating in Visible and Near Infrared (VNIR) and Short Wave Infrared (SWIR) regions, therefore covering the wavelength range between 400 and 2500 nm. Panchromatic (PAN) images are provided at higher spatial resolution in order to allow for image fusion techniques (i.e. "pan sharpening"). The Optical Head architecture is based on a common optical bench that accommodates the telescope on the upper side and the imaging spectrometers and panchromatic camera on the lower one. The common TMA telescope provides excellent optical quality with a minimum number of optical elements. The imaging spectrometer is based on a prism solution, in order to obtain high efficiency and low polarization sensitivity. The Payload is equipped with high performance VNIR and SWIR Focal Plane Array (FPA) detectors, which operate at a temperature around 188K (VNIR) and 189K (SWIR). The cooling is obtained by means of a passive radiator facing the cold space. The configuration is designed in order to match a detector array with a pixel size of 30 µm for both VNIR and SWIR channels, and 6.5 µm for the PAN. The detection chain involves three focal planes which are physically accommodated on the optical bench.

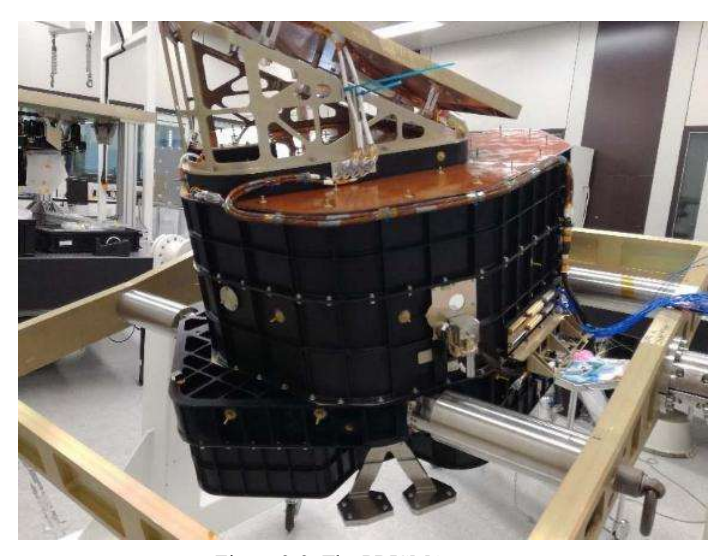


Figure 3-3. The PRISMA sensor

The Optical Head has two apertures that give access to the acquisition chain, the Main Ports and the Solar Ports. They are opened or closed using dedicated mechanisms. The Main Ports is the main aperture used for all Earth Observation acquisitions and for some types of Calibration acquisitions (i.e. Moon Calibration and External Flat Field Calibrations). These acquisitions follow the main optical path. The Solar Port is only used for Sun Calibration.

The instruments is managed by a Main Electronics (ME) box, which also handles power supply distribution and interfaces the Platform On Board Data Handling (OBDH) and

Payload Data Handling and Transmission (PDHT) modules. The ME manages telecommands and telemetries and channels the bit-stream carrying spectral images. It includes a data compression board to handle the high data volume related to the large number of supported spectral bands.

The Payload offers acquisition capabilities for Earth Observation in line with mission requirements and programmable in terms of active channels (VNIR, SWIR and Panchromatic), active bands and duration. Data acquired by the payload is transmitted to the Ground Segment and processed, resulting in PRISMA products that will be delivered to the end users, according to appropriate policies. Level 0 products carry raw scientific data and also include instrument and satellite ancillary data. They populate the PRISMA mission data catalogue. Level 1 products carry top-of-atmosphere radiometrically calibrated hyperspectral data. The data set includes co-registered panchromatic data. Besides Earth Observation capabilities the Payload offers a number of Calibration capabilities designed to ensure the maintenance of its performance along its lifecycle. Calibration takes place by means of the In-flight Calibration Unit (ICU) that allows the stimulation of the instrument with internal sources with a known spectral radiance (i.e. a lamp and a LED) and with radiation from Sun, through the Solar Port and a dedicated optical path that includes an integrating sphere. Additional calibration methods supported by the Payload are vicarious calibration, Moon calibration and External Flat Field calibration.

3.3 Ground segment

The PRISMA Ground Segment (GS) consists of the following main elements:

- MCC Mission Control Center;
- SCC Satellite Control Center;
- IDHS Image Data Handling Segment/Center.

The MCC consists of a unique subsystem, the Mission Planning System (MPS). It is the G/S element responsible for the scheduling of on board operations and for coordinating ground activities, performing overall mission planning, allocating resources and solving conflicts. The SCC includes the Satellite Control System (SCS), the Flight Dynamics System (FDS), the S-band TT&C Station (TT&C) and the G/S Network (Communication infrastructure connecting the PRISMA G/S centers and facilities). The IDHS is in charge of performing all the chain from the Users requests management to the delivery of final products, including reception of images data from the satellite and their processing. It includes different elements:

- Centro Nazionale Multimissione (CNM);
- L0 Processor;
- L1 Processor:

- L2 Processor;
- Calibration facility;
- GCP DB.

The CNM provides all ground segment functions related to catalogue browsing, image ordering from catalogue, standard products processing and product delivery. It includes the X-band ground station used to receive the payload data downloaded by the PRISMA satellite.

3.4 PRISMA Product

The Ground Segment data processing provides at Sensor Radiance (Level 1 products) or at Surface Radiance obtained by applying atmospheric correction (L2B product) and georeferencing/geolocation on reflectance data (L2C/2D products). Users can order new acquisition or catalogue products containing the TOA (Top Of Atmosphere) radiometrically and geometrically calibrated HYP and PAN radiance images and/or the BOA (Botton Of Athmosphere) Geolocated or Geocoded Atmospherically corrected HYP and PAN radiance or reflectance images. In detail the standard products which can be delivered to users, are:

- Level 0 (L0): Raw, uncalibrated sensor data with associated metadata. These products include instrument and satellite ancillary data and populate the mission data catalog. L0 products are associated with Key Data Parameters (KDPs) for further processing. L0 products are not provided to the users.
- Level 1 (L1): Radiometrically corrected and calibrated top-of-atmosphere (TOA)
 radiance data in physical units. L1 products include both hyperspectral and
 panchromatic data that are coregistered. The L1 data is formatted as HDF5 files
 with separate groups for science data, ancillary data, global attributes, and
 housekeeping information. Level 1 products are generated upon user request.
- Level 2B (L2B): At-surface radiance products in sensor geometry obtained by applying atmospheric corrections to Level 1 data. This includes data corrected for Rayleigh scattering, gaseous absorption, water vapor absorption, and aerosol scattering. Level 2B products are delivered with an attached geocoding model. L2B products are generated upon user request.
- Level 2C (L2C): Surface reflectance products with an attached geocoding model
 that are obtained by applying geometric and atmospheric corrections to L1 data.
 L2C products include an aerosol characterization product, water vapor map
 product, and cloud characterization. L2C products are generated upon user
 request.
- Level 2D (L2D): Geocoded surface reflectance products projected onto a cartographic UTM reference system. L2D products are orthorectified, with or

without the use of Ground Control Points (GCPs). L2D products are generated upon user request.

3.5 Orbit and coverage

PRISMA nominal orbit is a frozen Sun-synchronous orbit with repeat cycle of 29 days (430 orbits). The orbit mean altitude is about 614.8 Km with an inclination of 97.851°. The Local Time of Descending Node is 10.30 am. The orbit parameters are:

Table 3-2. PRISMA orbit parameters

| PARAMETER | VALUE |
|---------------------------|------------|
| Semi-major axis [km] | 6992.935 |
| Mean Altitude [km] | 614.8 |
| Eccentricity | 0. 0010566 |
| Inclination [deg] | 97.851 |
| Argument of Perigee [deg] | 90.0 |
| Period [seconds] | 5819.7 |
| Rev/days | 14.85 |
| Repetition factor | 14.83 |

The satellite will be able to pass over the same orbit within one month. Therefore, the orbit mission is designed in order to guarantee a repeating cycle shorter than 1 month, in particular, the baseline PRISMA orbit shall have a repeat time of 29 days.

The Primary area of interest considered includes almost all the main landmasses and is characterized by the following coordinates:

• Latitude: from 70° N to 70°S

• Longitude from 180°W to 180°E

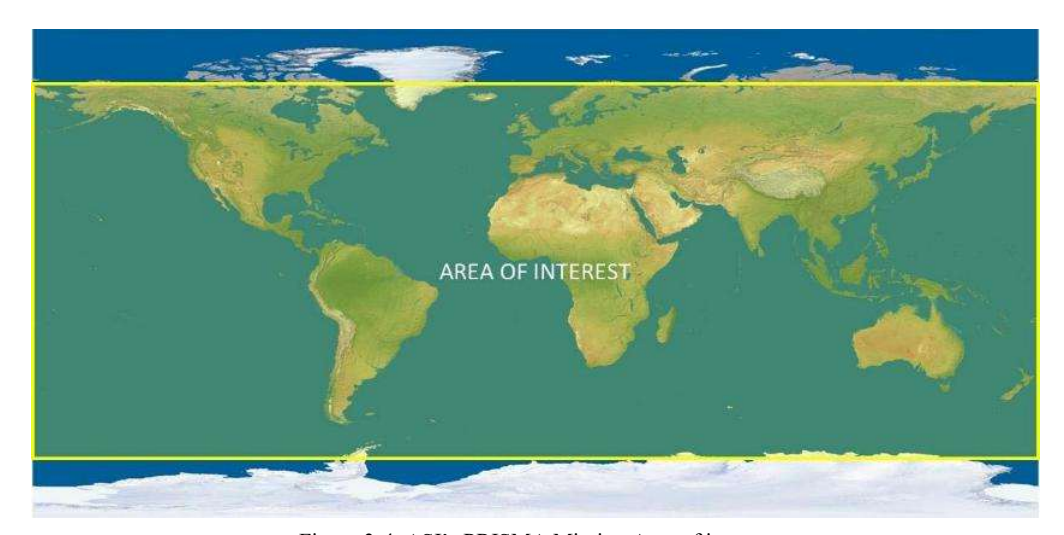


Figure 3-4. ASI's PRISMA Mission Area of interest

Chapter 4 Spectral Unmixing

4.1 Introduction to Hyperspectral Unmixing

Spectral unmixing is a fundamental technique in hyperspectral remote sensing, aimed at decomposing mixed spectral signatures into a set of pure spectral components, known as endmembers, and their corresponding fractional abundances. This process is essential for accurately identifying materials on the Earth's surface when pixel resolution is insufficient to isolate homogeneous materials. This is the case of PRISMA satellite, where every pixel is 30 x 30 m wide, resulting in likely multiple endmembers per pixel.

The spectral unmixing problem can be formally expressed as follows. Given an observed spectral vector $x \in R^L$, where L represents the number of spectral bands, the objective is to determine a set of endmembers $E = [e_1, e_2, ..., e_M] \in R^{L \times M}$ and corresponding abundance fractions $a \in R^M$, such that:

x = Ea + n, where *n* represents the noise term. The constraints $\sum_{i=1}^{M} a_i = 1$ and $0 \le a_i \le 1$ for all *i* ensure physical interpretability of the abundances.

4.2 Linear vs. Nonlinear Spectral Unmixing

Spectral unmixing techniques can be broadly classified into linear and nonlinear methods. The Linear Mixing Model (LMM) assumes that each pixel is a linear combination of endmember spectra, weighted by their respective abundances:

$$x = \sum_{i=1}^{M} a_i e_i + n (4.1)$$

LMM is widely used due to its mathematical simplicity and effectiveness in many real-world scenarios. However, in cases where multiple scattering effects and nonlinear interactions occur (e.g., in dense vegetation, urban areas, or water bodies), LMM fails to provide accurate results.

In contrast, Nonlinear Mixing Models (NMMs) incorporate higher-order interactions between endmembers. One common nonlinear model is the bilinear model:

$$x = \sum_{i=1}^{M} a_i e_i + \sum_{i=1}^{M} \sum_{j>i}^{M} a_i a_j e_i \odot e_j + n$$
 (4.2)

where \odot denotes element-wise multiplication. Other nonlinear models include radiative transfer models and kernel-based approaches.

4.3 Unsupervised Endmember Extraction

The extraction of endmembers is a critical step in spectral unmixing and can be categorized into supervised and unsupervised methods. In the following section we will describe some of the most common methods, some of which will be used in the proposed code (Chapter 5).

4.3.1 Principal Component Analysis (PCA)

Principal Component Analysis (PCA) is a statistical method widely used for dimensionality reduction and feature extraction in hyperspectral unmixing. It transforms high-dimensional spectral data into a lower-dimensional space while preserving the maximum variance in the dataset. By doing so, PCA enhances the separability of endmembers and reduces redundancy in hyperspectral images.

Given a hyperspectral dataset represented as a matrix $X \in \mathbb{R}^{L \times N}$, where L is the number of spectral bands and N is the number of pixels, the first step in PCA is to compute the meancentered data matrix:

$$X_c = X - \bar{X} \tag{4.3}$$

where \bar{X} represents the mean spectrum computed over all pixels. The covariance matrix C is then obtained as:

$$C = \frac{1}{N} X_c X_c^T \tag{4.4}$$

PCA proceeds by solving the eigenvalue problem:

$$CV = V\Lambda \tag{4.5}$$

where V is the matrix of eigenvectors (principal components) and Λ is the diagonal matrix of eigenvalues, which indicate the amount of variance explained by each principal component.

The principal components associated with the highest eigenvalues capture the most significant spectral variance in the dataset. In the context of spectral unmixing, PCA is used to:

1. Reduce Dimensionality: Selecting the top *M* principal components instead of using all *L* bands improves computational efficiency.

- 2. Enhance Endmember Separability: Endmembers tend to cluster along specific principal components, making it easier to identify pure spectra.
- 3. Noise Reduction: By discarding components associated with small eigenvalues, PCA eliminates noise while retaining essential spectral features.

After applying PCA, a common approach for endmember extraction is to identify pixels that exhibit extreme values in the transformed space, assuming that pure spectral signatures correspond to these extremities.

4.3.2 Vertex Component Analysis (VCA)

A widely used approach that assumes endmembers are the vertices of a convex hull in spectral space. VCA exploits the affine transformation property of LMM to iteratively identify extreme spectral signatures. It is based on the assumption that the spectral signatures of endmembers form a convex simplex in the spectral space. VCA exploits the affine transformation property of the LMM to iteratively identify the most extreme spectral signatures.

Given a hyperspectral dataset $X \in R^{L \times N}$, where L is the number of spectral bands and N is the number of pixels, VCA aims to identify a set of M endmembers $E = [e_1, e_2, ..., e_M] \in R^{L \times M}$ such that:

$$\mathbf{x_i} \approx \sum_{j=1}^{M} a_{ij} \mathbf{e_j}$$
, with $\sum_{j=1}^{M} a_{ij} = 1$ and $a_{ij} \ge 0$ (4.6)

The steps of the VCA algorithm are the following:

1. Whitening the Data: The hyperspectral data X is first transformed using Principal Component Analysis (PCA) to reduce redundancy and enhance computational efficiency. The data is projected onto a subspace of dimension M-1:

$$X_{w} = WX \tag{4.7}$$

where W is the whitening transformation matrix derived from the covariance matrix of X.

 Random Projections: VCA exploits the property that endmembers lie at the extrema of the data cloud. A series of random projection vectors r_k are used to iteratively identify these extrema:

$$p^{(k)} = X_w^T r_k \tag{4.8}$$

The pixel corresponding to the maximum projection value is selected as a candidate endmember.

3. Deflation Process: Once an endmember is identified, the data is projected onto the subspace orthogonal to the identified endmember to prevent reselection. Given an identified endmember e_i, the deflation process is performed as:

$$X_{w} = (I - e_{i}e_{i}^{T}) \tag{4.9}$$

Iterative Endmember Selection: Steps 2 and 3 are repeated until M endmembers have been selected. The final set of endmembers is transformed back to the original spectral space using the inverse whitening transformation:

$$E = W^{-1}E_{w} (4.10)$$

Between VCA's advantages it is worth mentioning that it is usually computationally efficient and it does not require prior knowledge of the number of endmembers. However, there are also some limitations, including the fact that it assumes that pure endmembers exist within the dataset, which may not always be true. Additionally, this method is sensitive to noise and variations in spectral signatures.

4.3.3 Pixel Purity Index (PPI)

The Pixel Purity Index (PPI) is a widely used method for unsupervised endmember extraction in hyperspectral unmixing. It is based on the assumption that pure spectral signatures appear as extreme points in high-dimensional spectral space. By repeatedly projecting spectral data onto randomly generated unit vectors, PPI identifies the pixels that most frequently appear as extrema.

Given a hyperspectral dataset $X \in R^{L \times N}$, where L is the number of spectral bands and N is the number of pixels, the PPI method follows these steps:

Data Projection: for each random unit vector r_k , project all spectral vectors x_i onto r_k :

$$p_{i}^{(k)} = x_{i}^{T} r_{k} \tag{4.11}$$

Extreme Point Identification: identify the pixels corresponding to the maximum and minimum projection values:

$$i_{max} = \arg \max_{i} p_i^{(k)}, \qquad i_{min} = \arg \min_{i} p_i^{(k)}$$
 (4.12)

Repetition: repeat the process for K randomly chosen projection vectors. Maintain a counter for each pixel that tracks the number of times it appears as an extreme point.

Thresholding: Select pixels that exceed a predefined threshold as candidate endmembers. These are considered the purest spectral signatures in the dataset.

PPI is a simple and effective method for datasets with distinct pure pixels and it does not require prior knowledge of the number of endmembers. However, it is usually computationally expensive due to the need for a large number of projections and it is sensitive to noise and outliers, which can affect the selection of pure pixels.

4.3.4 N-FINDR

N-FINDR is a widely used unsupervised endmember extraction algorithm based on the geometric principle that the simplex with the largest volume enclosing the data points in spectral space corresponds to the optimal set of endmembers. It operates under the assumption of a LMM, where each observed spectral pixel can be expressed as a convex combination of endmembers.

Given a hyperspectral dataset $X \in R^{L \times N}$, where L is the number of spectral bands and N is the number of pixels, N-FINDR seeks to determine a set of M endmembers $E = [e_1, e_2, ..., e_M] \in R^{L \times M}$ such that they maximize the volume of the simplex defined by the endmembers.

The volume V of a simplex formed by M endmembers in an L-dimensional space is given by:

$$V = \frac{1}{(M-1)!} |\det([e_2 - e_1, e_3 - e_1, ..., e_M - e_1])|$$
 (4.13)

N-FINDR aims to iteratively refine the selection of endmembers to maximize this volume, using the following steps:

- 1. initialize endmembers: randomly select M pixels from the dataset as an initial set of endmembers;
- 2. volume calculation: compute the volume of the simplex formed by the current set of endmembers using the determinant-based formula;
- 3. pixel substitution: for each candidate endmember position j, replace e_j with every other pixel in X and recompute the volume.
- 4. if a new pixel increases the simplex volume, update the endmember set with this new pixel.
- 5. iterate until convergence: repeat step 3 until no further volume increase is observed.

N-FINDR is an efficient and deterministic method for identifying endmembers, that ensures maximal separability of extracted endmembers. However, we can mention between its limitations that it is sensitive to noise and outliers, as extreme values can dominate selection. Additionally, it is computationally expensive for large datasets due to iterative volume computations.

4.4 Supervised Endmember Extraction

In contrast to unsupervised methods, supervised approaches rely on reference spectral libraries, ground truth data, or prior knowledge to guide the extraction process. These include:

1. Spectral Angle Mapper (SAM): Measures the similarity between observed spectra and reference endmembers using the spectral angle distance.

2. Support Vector Machines (SVMs): Classify spectral data based on labeled training samples, enabling robust endmember selection.

4.5 Advanced Spectral Unmixing Techniques

4.5.1 Autoencoders for Spectral Unmixing

Autoencoders (AEs) are neural network architectures designed for unsupervised feature learning, particularly suited for hyperspectral unmixing. They consist of two primary components: an encoder that compresses input data into a latent representation and a decoder that reconstructs the original data from this compressed representation. The objective is to learn an optimal transformation that captures the underlying spectral characteristics of the data while reducing noise and redundancy.

Given an input spectral vector $\mathbf{x} \in \mathbf{R}^{\mathbf{L}}$, an autoencoder consists of an encoder function $f_{\theta} \colon \mathbf{R}^{L} \to \mathbf{R}^{d}$ and a decoder function $g_{\phi} \colon \mathbf{R}^{d} \to \mathbf{R}^{L}$, where d is the dimensionality of the latent space, and θ , ϕ are the learned parameters. The encoding and decoding processes are defined as:

$$z = f_{\theta}(x) = \sigma(W_{e}x + b_{e}), \quad \hat{x} = g_{\phi}(z) = \sigma(W_{d}z + b_{d})$$
 (4.14)

where $W_e \in R^{d \times L}$ and $W_d \in R^{L \times d}$ are the weight matrices of the encoder and decoder, respectively, $b_e \in R^d$ and $b_d \in R^L$ are bias terms, σ is a non-linear activation function such as ReLU or sigmoid. The loss function for training an autoencoder is typically the reconstruction error, given by the mean squared error (MSE):

$$L(\theta, \phi) = \frac{1}{N} \sum_{i=1}^{N} ||x_i - \hat{x}_i||^2$$
 (4.15)

where *N* is the number of training samples.

For hyperspectral unmixing, the latent representation z is interpreted as the abundance vector a, constrained such that a satisfies non-negativity and sum-to-one conditions. This can be achieved using a softmax activation function:

$$a_i = \frac{e^{z_i}}{\sum_{i=1}^{M} e^{z_i}} \tag{4.16}$$

The endmember matrix E can be learned as part of the decoder weights, allowing the network to extract representative spectral signatures directly from the data.

Autoencoders techniques are able to Learn non-linear feature representations, improving unmixing in complex scenarios. Additionally, they can incorporate physical constraints like sum-to-one and non-negativity. However, they require large datasets for training to avoid overfitting, and they are computationally expensive compared to traditional linear methods.

4.5.2 Convolutional Neural Networks (CNNs)

Convolutional Neural Networks (CNNs) have emerged as powerful tools for hyperspectral unmixing, particularly in scenarios where spatial dependencies between pixels provide additional information. Unlike fully connected networks, CNNs exploit local patterns in spectral data, making them particularly suited for extracting spectral-spatial features.

A CNN consists of multiple layers, including convolutional layers, activation functions, pooling layers, and fully connected layers. The convolutional operation applied to an input hyperspectral image X is given by:

$$F_{i,j}^{(l)} = \sigma \left(\sum_{m=1}^{M} \sum_{p=1}^{P} \sum_{q=1}^{Q} W_{m,p,q}^{(l)} X_{i+p,j+q}^{(l-1)} + b^{(l)} \right)$$
(4.17)

where:

 $F_{i,j}^{(l)}$ is the feature map at position (i,j) in layer l, $W_{m,p,q}^{(l)}$ is the convolutional kernel of size $P \times Q$ applied to input m, $b^{(l)}$ is the bias term, σ is an activation function (e.g., ReLU or sigmoid).

Following the convolutional layer, pooling layers are used to reduce dimensionality while retaining critical spectral-spatial features:

$$F_{i,j}^{(l)} = \max_{p,q} F_{i+p,j+q}^{(l-1)} \tag{4.18}$$

where max-pooling selects the maximum value in a given window $p \times q$, improving computational efficiency and robustness.

For spectral unmixing, CNNs are trained to extract spatial and spectral correlations to improve endmember and abundance estimation. Given an input hyperspectral image X, CNNs predict the abundance maps A by learning hierarchical representations:

$$A = f(X; \theta) \tag{4.19}$$

where f represents the CNN function parameterized by weights θ . The network is trained using a loss function, such as the mean squared error (MSE):

$$L(\theta) = \frac{1}{N} \sum_{i=1}^{N} |A_i - \widehat{A}_i|^2$$
 (4.20)

Between the advantages of using CNNs we can mention the ability to capture spatial dependencies, improving robustness in mixed-pixel scenarios. Additionally, CNNs can model nonlinearity more effectively than traditional methods and they are able to reduce spectral variability by leveraging spatial information. On the other hand, CNNs are computationally expensive, requiring significant processing power.

Chapter 5 Proposed Unmixing Code

The proposed unmixing code uses a mix of multiple techniques in order to obtain robust solutions independently with respect to the selected scenarios. Additionally, the use of a limited subset allows to reduce the computational time and obtain useful results in few hours also using a consumer grade laptop. More in detail, the code starts importing the hyperspectral image and associating the bands numbers with the PRISMA's wavelength. In the following part the actual unmixing process takes place, with the initialization of the endmembers (using VCA, PCA and N-FINDR techniques), in order to provide robust inputs to the Convolutional Neural Network (CNN). The network is trained and fine-tuned using two randomly selected sub-sets. The last phase, before plotting results, associates the computed endmembers with the library from NASA Jet Propulsion Laboratory (JPL), using a mix of Spectral Angle Mapper (SAM) and Spectral Information Divergence (SID) techniques in order to select the most "similar" material from the library.

5.1 Data Preprocessing

The code starts by reading the PRISMA satellite data from an HDF5 file. The data consists of two cubes: VNIR (Visible and Near-Infrared, 66 bands) and SWIR (Short-Wave Infrared, 173 bands). These cubes are concatenated along the spectral dimension to form a single hyperspectral data cube.

```
swirData = double(h5read(inputFile, swirPath));
vnirData = double(h5read(inputFile, vnirPath));
data = cat(2, vnirData, swirData);
```

5.2 Band-Wavelength Association

The code reads an Excel file containing the band numbers and their corresponding wavelengths. The wavelengths are sorted in ascending order, and the band numbers are rearranged accordingly.

```
[num, txt, raw] = xlsread(excelFile);
band_numbers_VNIR = num(1:66, 1);
wavelengths_VNIR = num(1:66, 2);
band_numbers_SWIR = num(67:end, 1);
wavelengths_SWIR = num(67:end, 4);
band_numbers = [band_numbers_VNIR; band_numbers_SWIR];
wavelengths = [wavelengths_VNIR; wavelengths_SWIR];
[wavelengths_sorted, sortIdx] = sort(wavelengths);
band_numbers_sorted = band_numbers(sortIdx);
```

5.3 Hyperspectral Unmixing

5.3.1 Endmember Initialization

The code initializes endmembers using three techniques: N-FINDR, VCA, and PCA.

- N-FINDR: This algorithm finds the simplex of maximum volume that can be inscribed within the data cloud. The vertices of this simplex are considered as endmembers.
- VCA: Vertex Component Analysis is a geometric approach that projects the data onto a subspace and then iteratively finds the vertices of the simplex.
- PCA: Principal Component Analysis reduces the dimensionality of the data by projecting it onto the principal components. The endmembers are then extracted from the reduced space.

```
endmembers_init1_nf = nf_findr(X1', num_endmembers);
endmembers_init1_vca = vca(X1', num_endmembers);
endmembers_init1_pca = pca_endmembers(X1', num_endmembers);
```

5.3.2 CNN for Endmember Extraction

A Convolutional Neural Network (CNN) is used to refine the endmembers. The CNN is trained on a subset of the data, where the input is the spectral data and the output is the initial abundance estimates. The CNN architecture can be described as follows:

- Input Layer: Accepts the spectral data reshaped into a 4D tensor.
- Convolutional Layer: Applies a 3x3 convolution with 16 filters.
- ReLU Activation: Introduces non-linearity.
- Fully Connected Layer: Maps the features to the number of endmembers.
- Regression Layer: Outputs the abundance estimates.

```
layers = [
  imageInputLayer([1 1 size(X1, 2)])
  convolution2dLayer(3, 16, 'Padding', 'same')
  reluLayer
  fullyConnectedLayer(num_endmembers)
  regressionLayer];
```

The CNN is trained using the Adam optimizer with a learning rate of 1e⁻³ for 500 epochs.

```
options = trainingOptions('adam', ...
    'MaxEpochs', 500, ...
    'MiniBatchSize', 32, ...
    'InitialLearnRate', 1e-3, ...
    'Verbose', false, ...
    'Plots', 'training-progress');
net1 = trainNetwork(X1_cnn, Y1, layers, options);
```

5.3.3 Abundance Estimation using Isquonneg

The non-negative least squares (Isqnonneg) method is used to estimate the abundances of the endmembers. This method solves the following optimization problem:

$$\min_{A} |X - EA|_2^2 \text{ subject to } A \ge 0$$
 (5.1)

where (X) is the observed spectral data, (E) is the endmember matrix, and (A) is the abundance matrix.

```
for i = 1:size(X1, 1)
    abundances_init1(i, :) = lsqnonneg(endmembers_init1, X1(i, :)')';
end
```

5.4 Spectral Library Import

The code imports a spectral library from JPL, which contains spectral signatures of various materials. The library is read from text files, and the reflectance values are normalized.

```
files = dir(fullfile(libraryFolder, '*.txt'));
for i = 1:length(files)
    filename = fullfile(libraryFolder, files(i).name);
    fileID = fopen(filename, 'r');
    line = fgetl(fileID);
    name = strtrim(strrep(line, 'Name: ', ''));
    data = textscan(fileID, '%f %f', 'HeaderLines', 21);
    fclose(fileID);
    reflectance_normalized = data{2} / 100;
    library_spectra(i).name = name;
    library_spectra(i).wavelength = data{1} * 1000;
    library_spectra(i).reflectance = reflectance_normalized;
end
```

5.5 Endmember Comparison

The extracted endmembers are compared with the spectral library using Spectral Angle Mapper (SAM) and Spectral Information Divergence (SID).

- SAM: Measures the spectral similarity between two spectra by calculating the angle between them in the spectral space.

$$SAM(s_1, s_2) = \cos^{-1}\left(\frac{s_1 \cdot s_2}{|s_1||s_2|}\right)$$
 (5.2)

- -SID: Measures the divergence between two probability distributions derived from the spectra.

$$SID(s_1, s_2) = D(s_1|s_2) + D(s_2|s_1)$$
(5.3)

where $(D(s_1|s_2))$ is the Kullback-Leibler divergence.

```
for i = 1:num_endmembers
   extracted = endmembers_original_space(:, i);
    extracted_norm = extracted / norm(extracted);
    for j = 1:length(library_spectra)
       library_interp = interp1(library_spectra(j).wavelength, ...
                            library_spectra(j).reflectance, ...
                            prisma_wavelengths, 'spline', 'extrap');
       library_norm = library_interp / norm(library_interp);
       dot_product = dot(extracted_norm, library_norm);
       norm_product = norm(extracted_norm) * norm(library_norm);
       if norm_product > 0
           sam_values(i, j) = acos(max(-1, min(1, dot_product)))
norm_product)));
       else
           sam_values(i, j) = NaN;
       end
       sid_values(i,
                              spectral_information_divergence(extracted,
                       j) =
library_interp);
   end
end
```

Chapter 6 Results

6.1 Identified Endmembers

The proposed code correctly extracted 12 different endmembers. Their spectral signatures were plotted in terms of normalized reflectance vs. wavelength (Figure 6-1, Figure 6-2 and Figure 6-3), as defined by PRISMA specification. In order to be sure that the extracted endmembers were actually different between each other, the cross-correlation values were calculated (Figure 6-4).

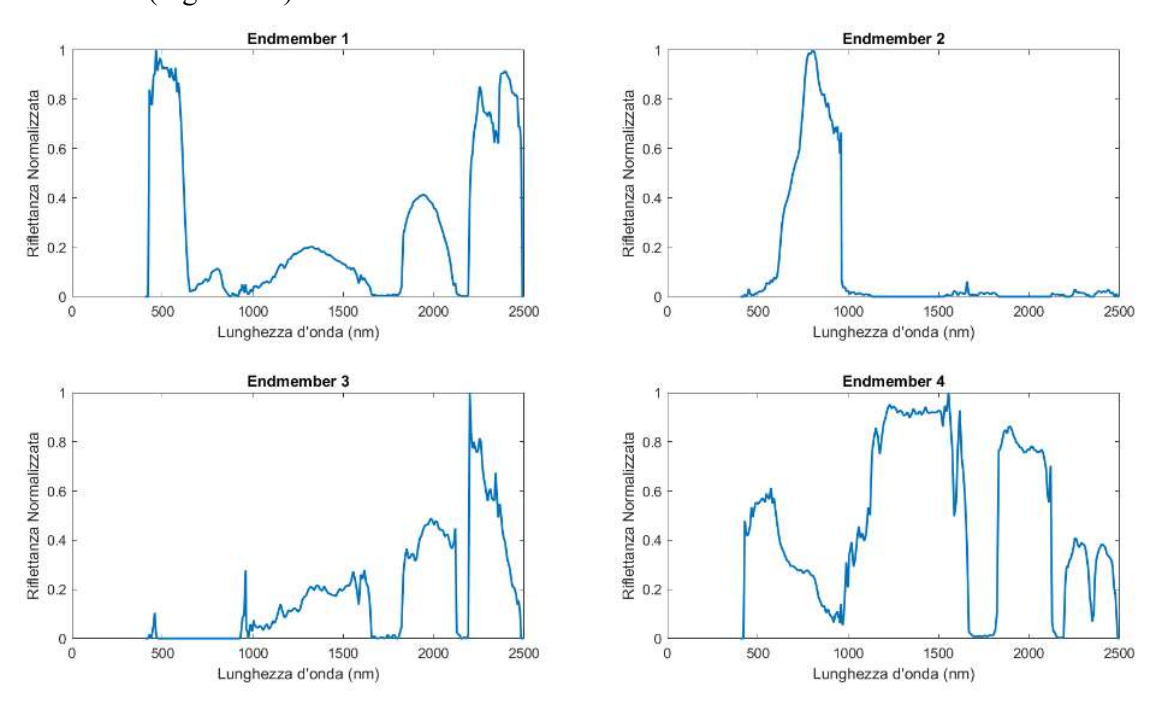


Figure 6-1. Spectral signatures – Endmembers 1 to 4

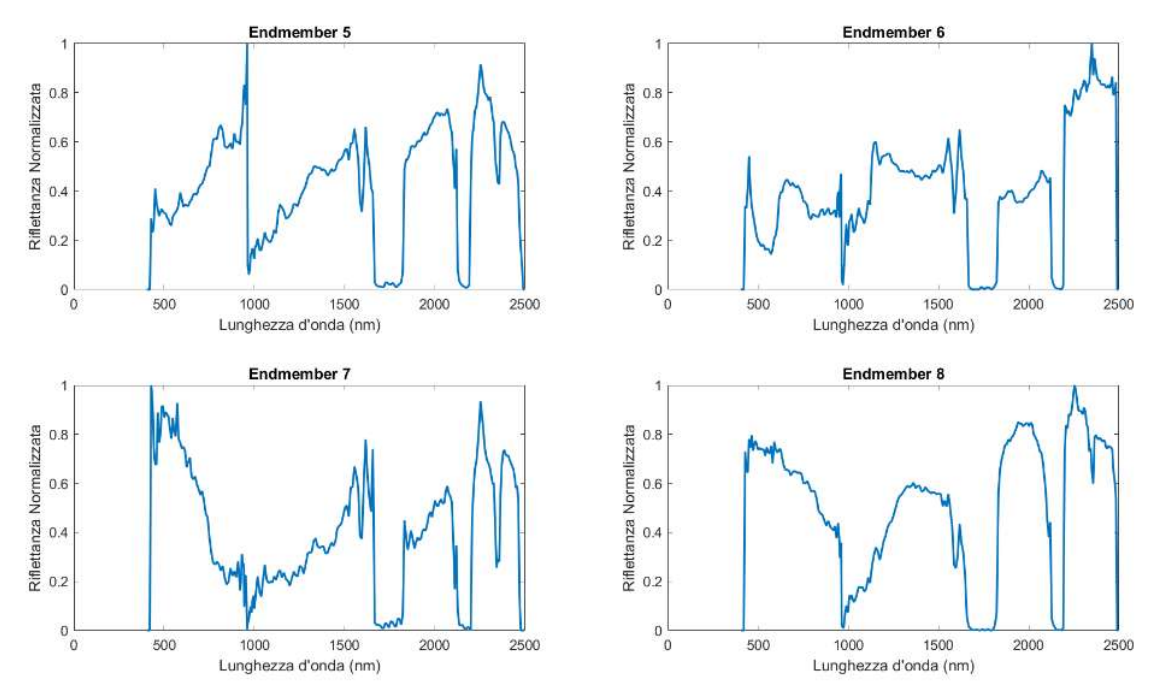


Figure 6-2. Spectral signatures – Endmembers 5 to 8

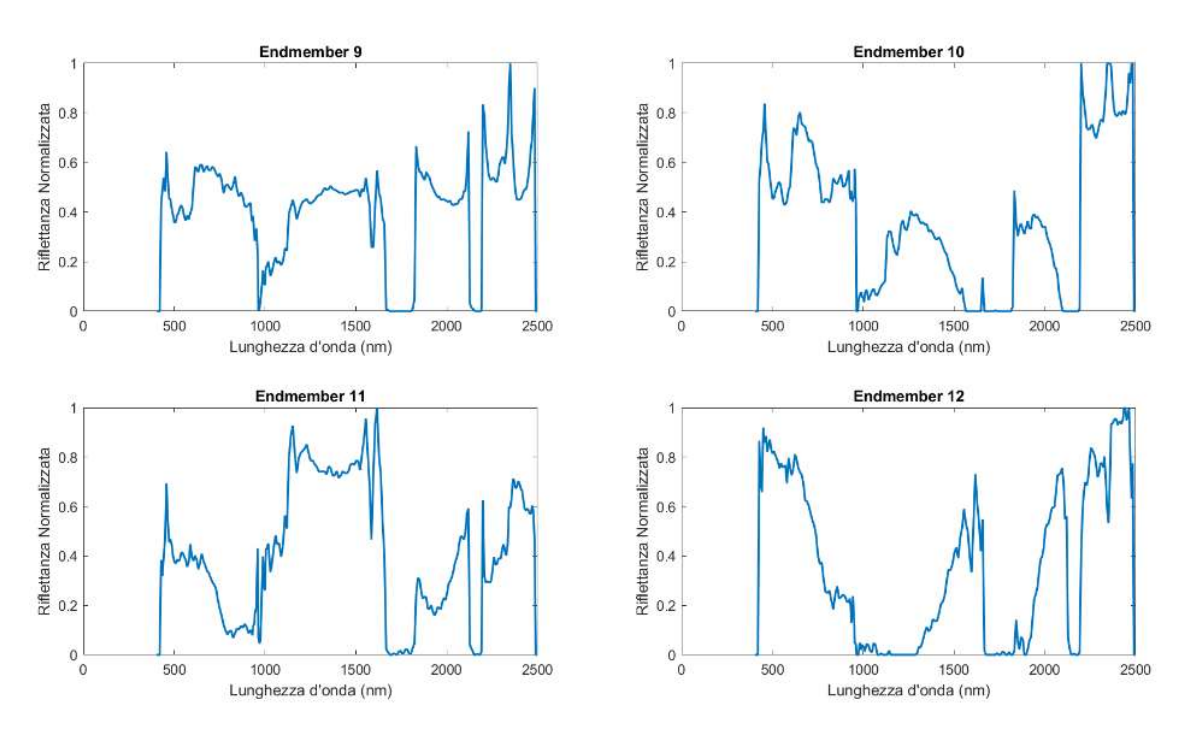


Figure 6-3. Spectral signatures – Endmembers 9 to 12

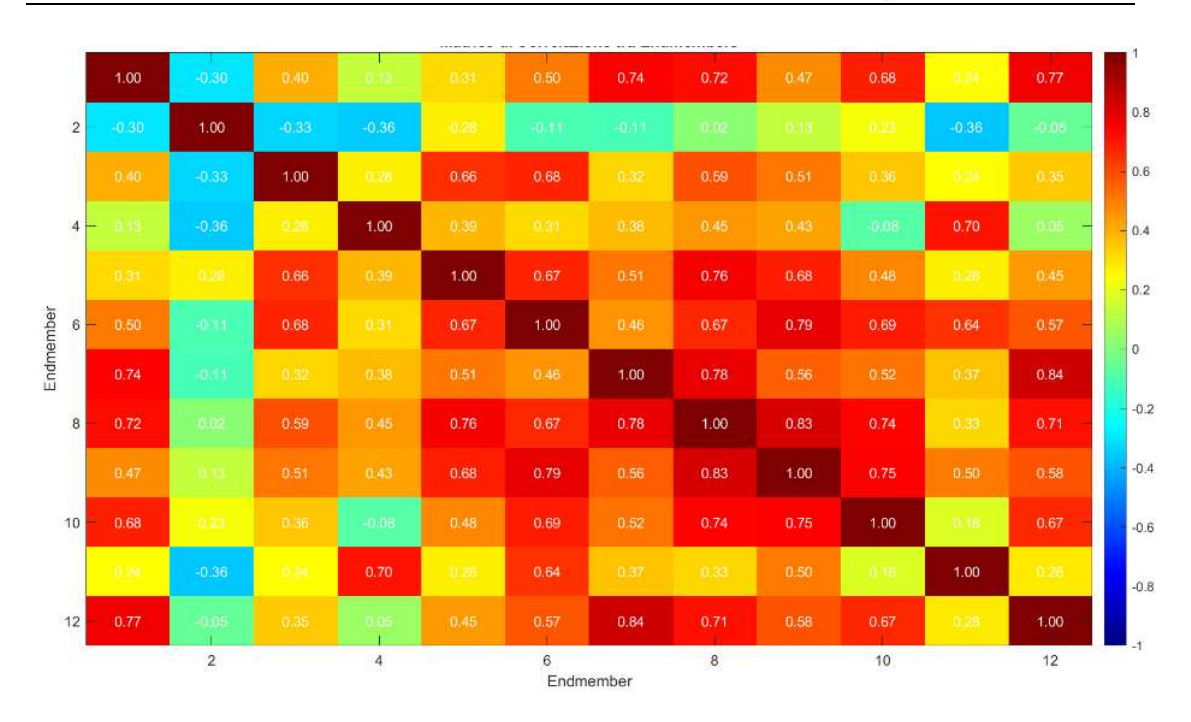


Figure 6-4. Endmembers' spectra cross-correlations.

6.2 Abundances

Following endmembers extraction, the relative abundances were plotted. Abundances maps confirm visually that the identified endmembers are actually different, since their presence on the ground might be associated with different structures, human-made features and natural elements.

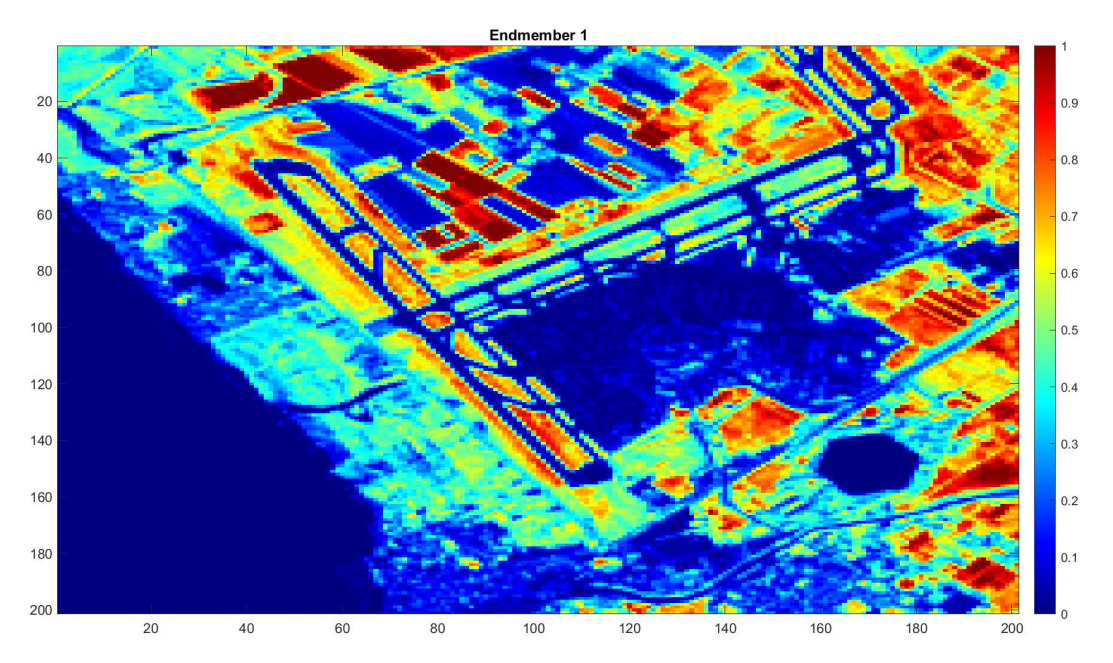
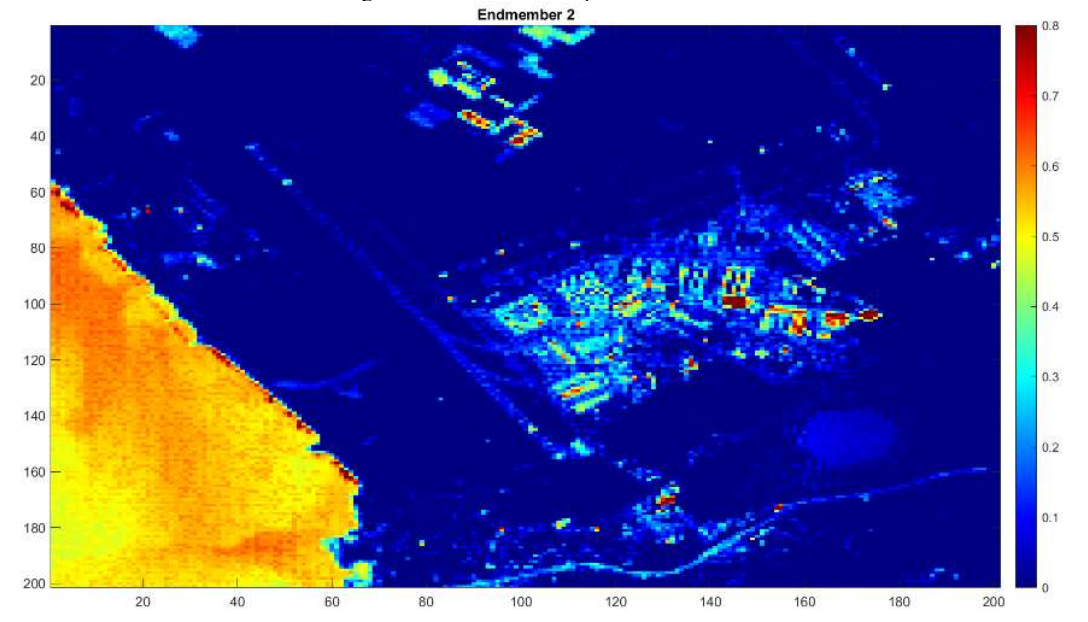


Figure 6-5. Abundance map – Endmember 1



 $Figure\ 6\text{-}6.\ Abundance\ map-Endmember\ 2$

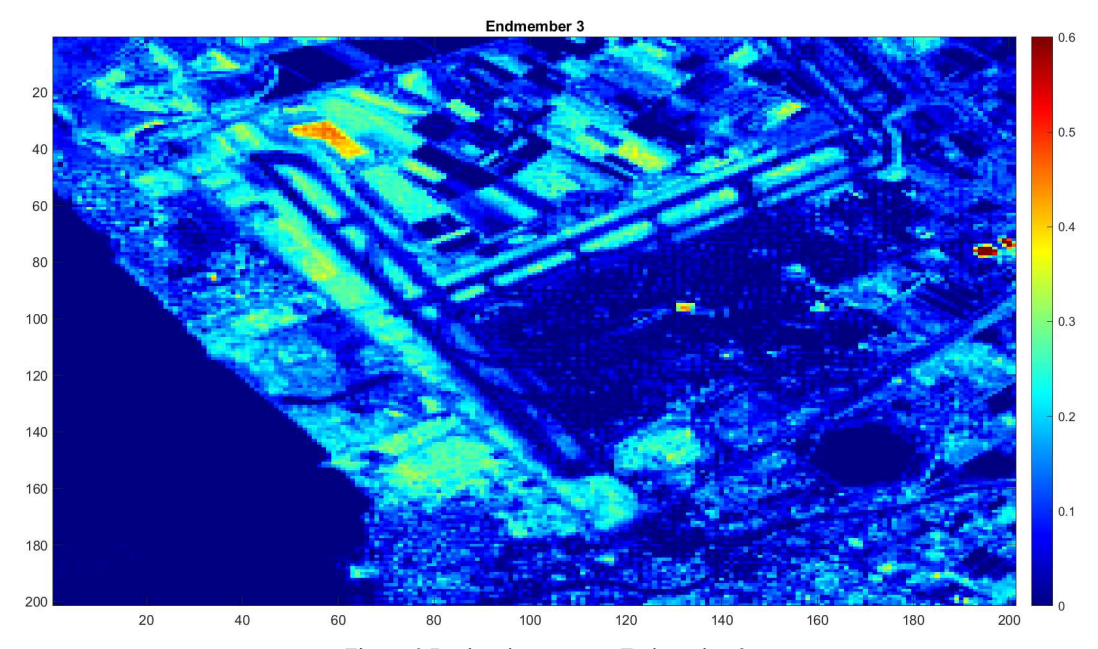


Figure 6-7. Abundance map – Endmember 3

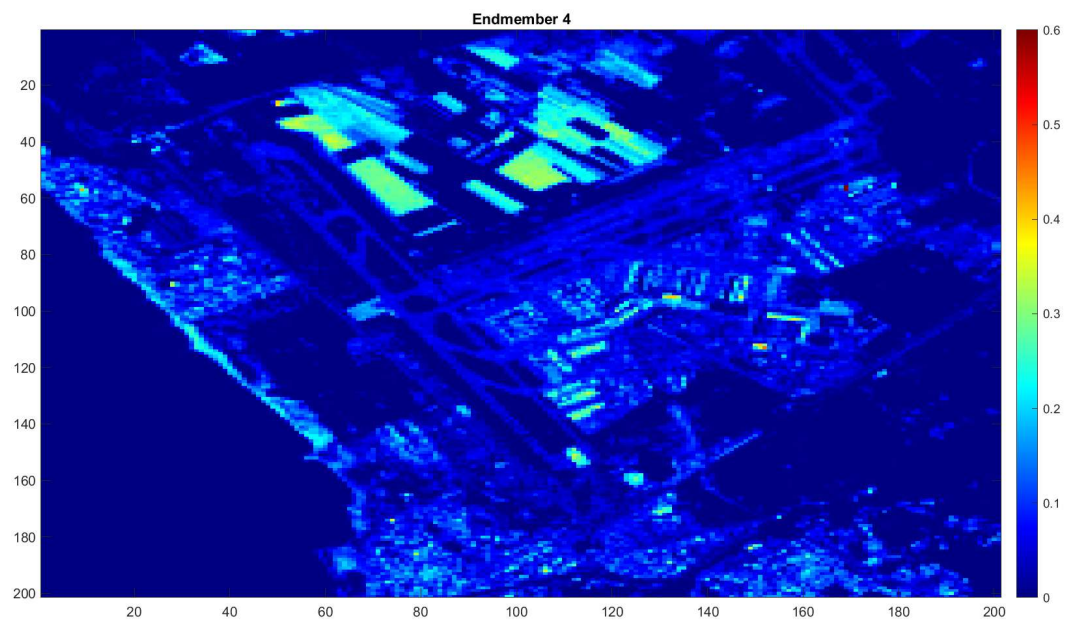


Figure 6-8. Abundance map – Endmember 4

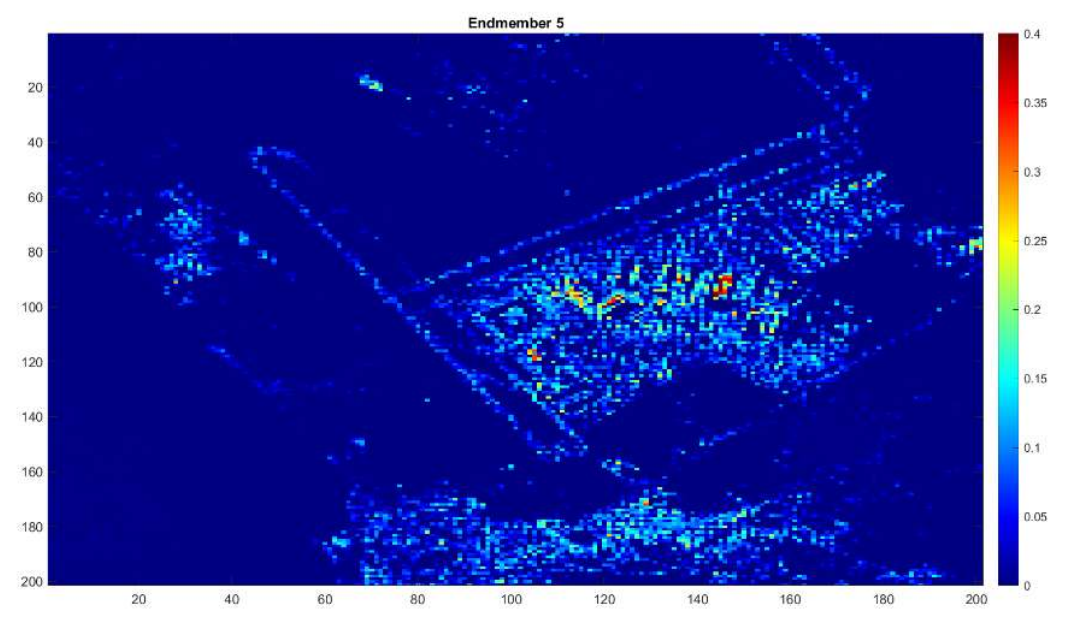
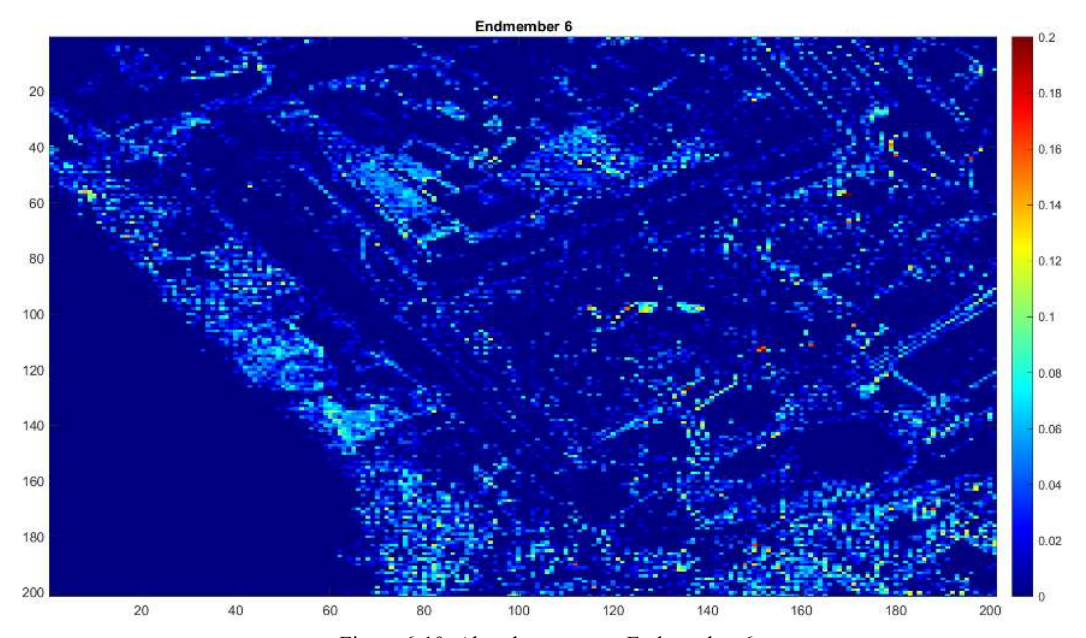


Figure 6-9. Abundance map – Endmember 5



 $Figure\ 6\text{--}10.\ Abundance\ map-Endmember\ 6$

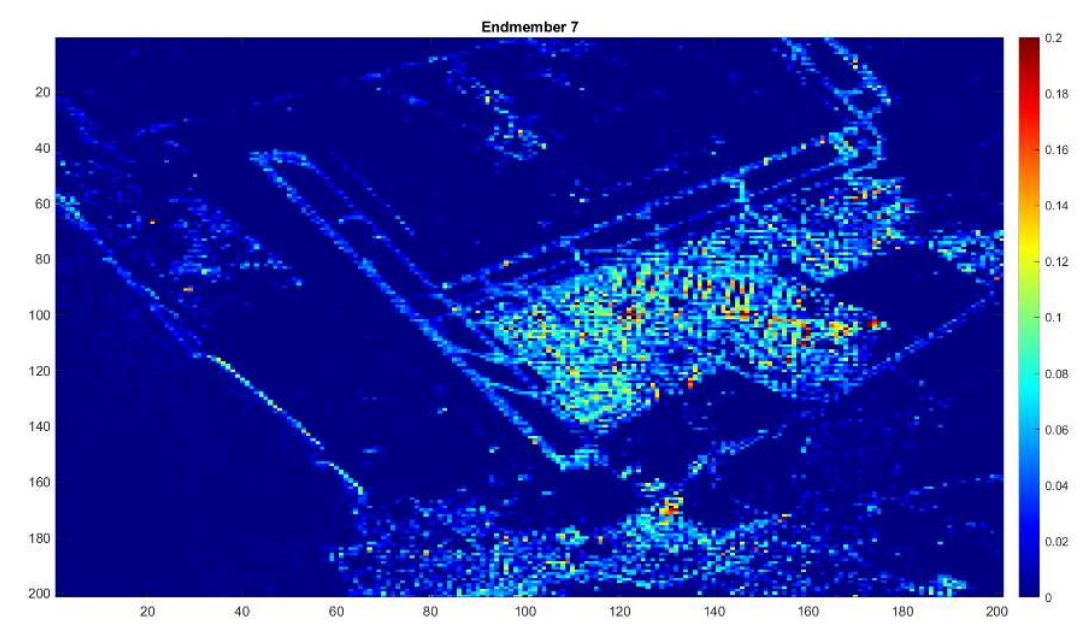


Figure 6-11. Abundance map – Endmember 7

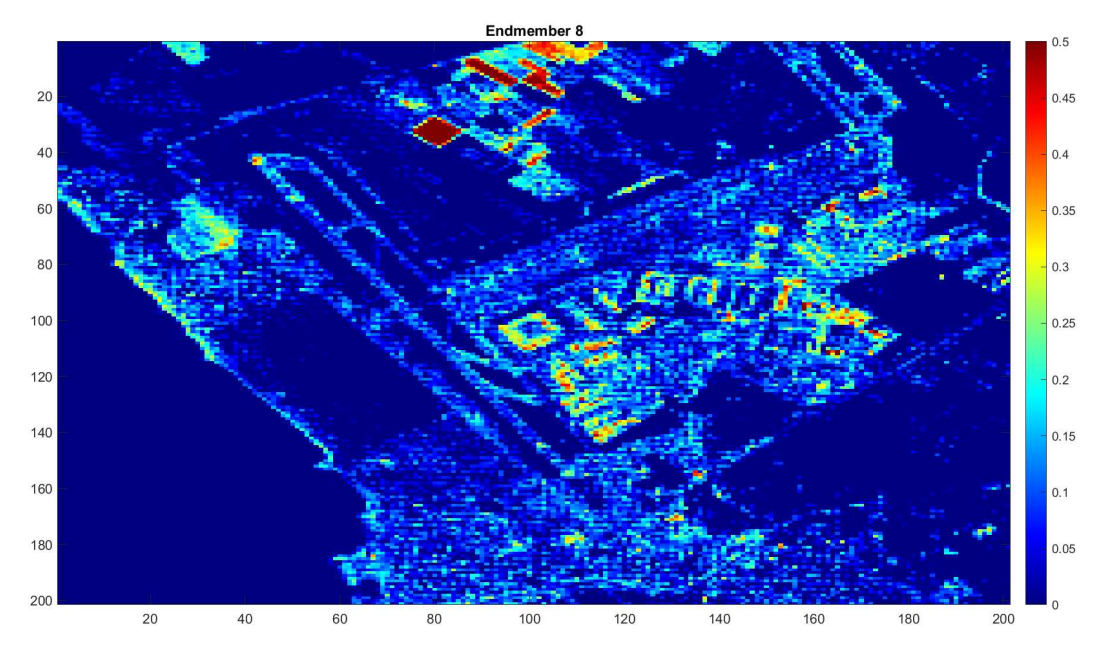


Figure 6-12. Abundance map – Endmember 8

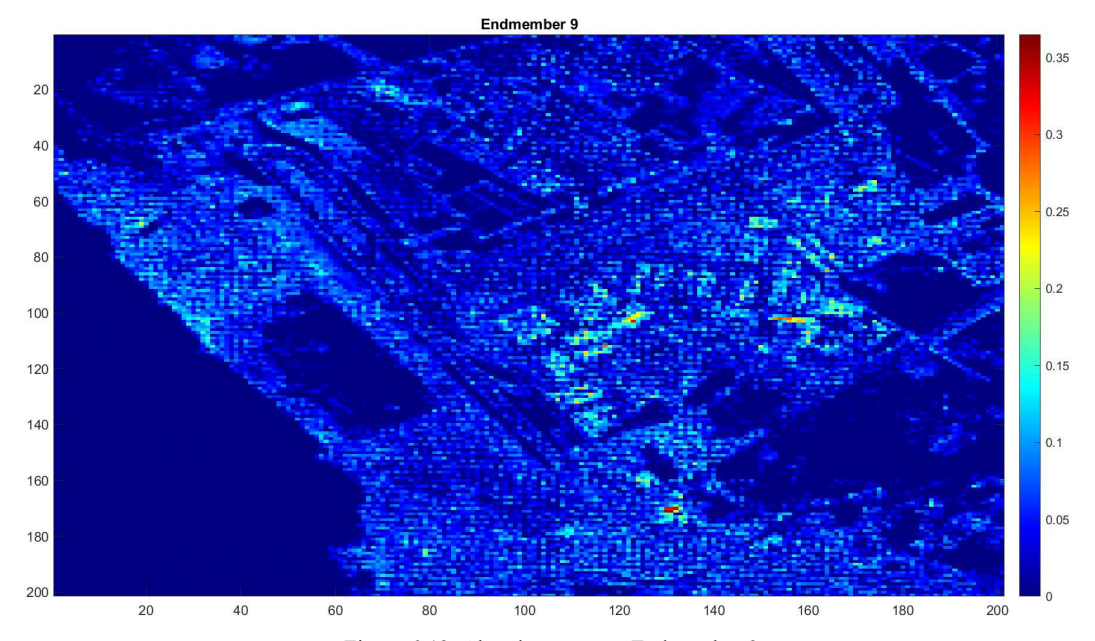


Figure 6-13. Abundance map – Endmember 9

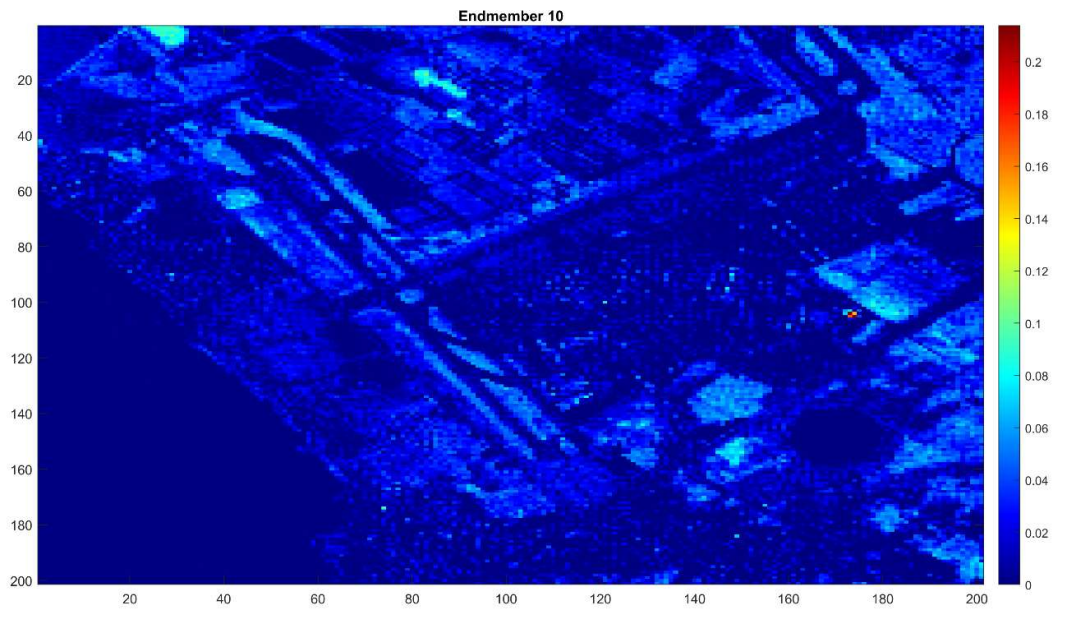


Figure 6-14. Abundance map – Endmember 10

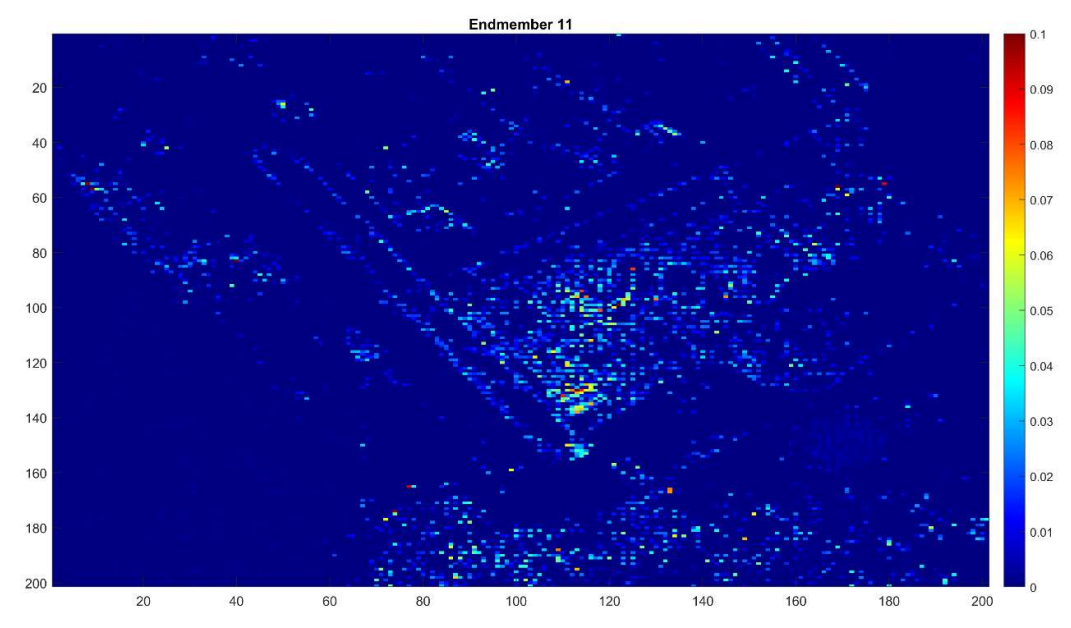
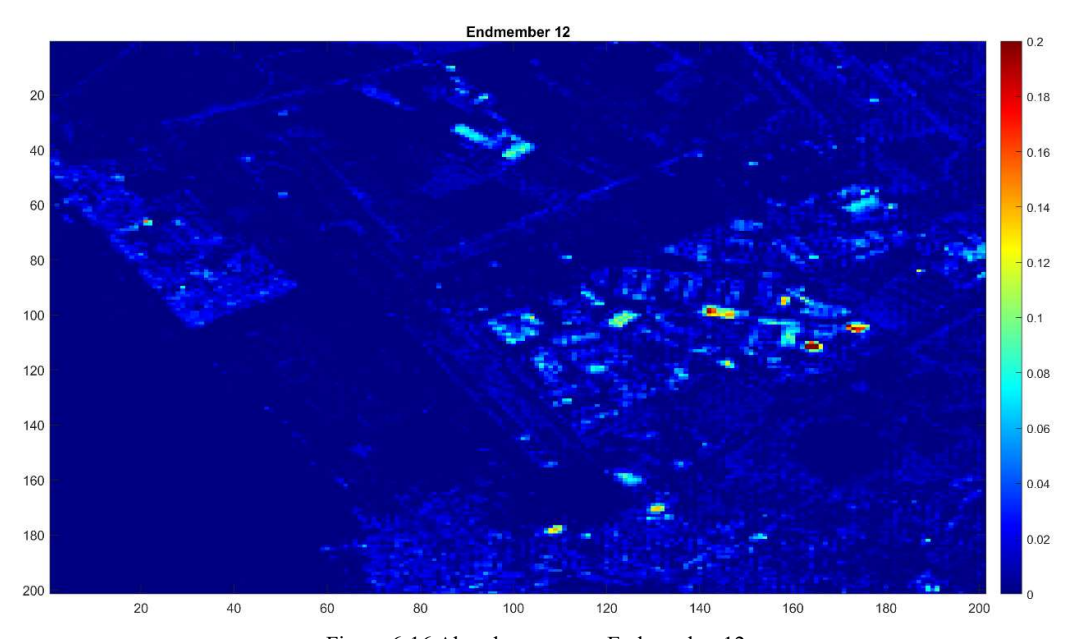


Figure 6-15. Abundance map – Endmember 11



 $Figure\ 6\text{-}16\ Abundance\ map-Endmember\ 12$

6.3 Model validation

The limit of PRISMA data is the current lack of dedicated campaigns to cross-corelate measures with ground truth data. In order to mitigate this limitation, the proposed model was tested against other hyperspectral data, aiming to verify that it is able to isolate multiple endmembers and consistently associate them to different classes.

Specifically, the model was tested against the Pavia University hyperspectral image acquired by the ROSIS sensor during a flight campaign over Pavia, northern Italy. The data is publicly available on Group De Inteligencia Computacional (GIC).

The Pavia university HSI has 103 spectral bands, and It contains 610 x 340 pixels, but spectral samples of the image contain no information about the wavelengths. The geometric resolution is 1.3 meters. The groundtruth of the HSI is differentiated into 9 classes.

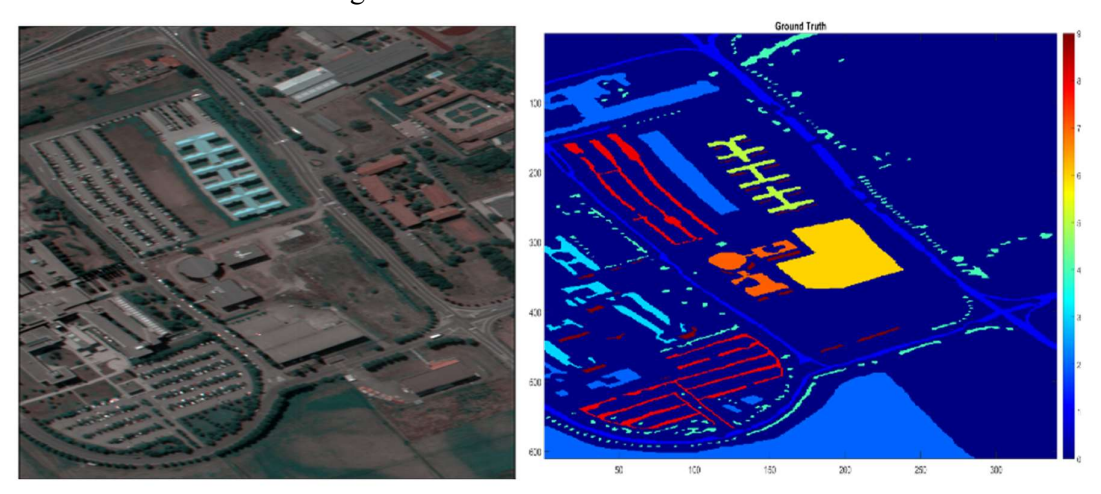


Figure 6-17. University of Pavia – Pancromatic (left) vs Hyperspectral classes (right)
Table 6-1. Groundtruth classes for the Pavia University scene and their respective samples number

| # | Class | Samples |
|---|----------------------|---------|
| 1 | Asphalt | 6631 |
| 2 | Meadows | 18649 |
| 3 | Gravel | 2099 |
| 4 | Trees | 3064 |
| 5 | Painted metal sheets | 1345 |
| 6 | Bare Soil | 5029 |
| 7 | Bitumen | 1330 |
| 8 | Self-Blocking Bricks | 3682 |
| 9 | Shadows | 947 |

Even with the described limitation in terms of unknown wavelengths associated with the bands, it was possible to extract twelve endmembers from a subset of 200 x 200 pixel of the University of Pavia data.

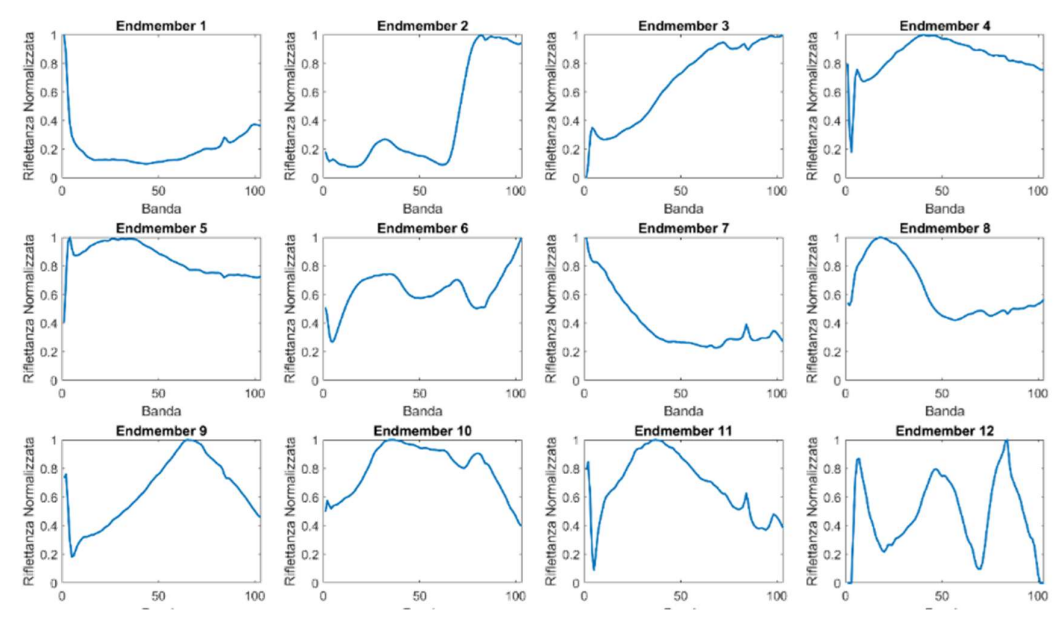


Figure 6-18. Endmembers extracted by the proposed model from University of Pavia Data

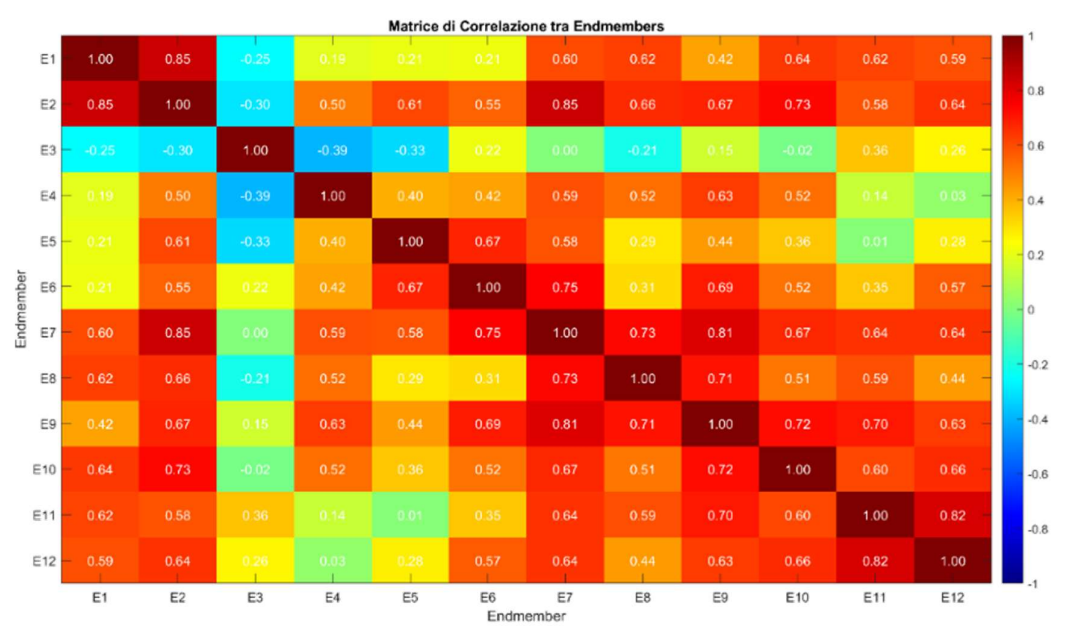


Figure 6-19. Endmember cross-correlation (University of Pavia Dataset)

As depicted in the Figure 6-20 to Figure 6-22, the proposed model correctly separates the different classes, in accordance with the expected results from ground truth data.

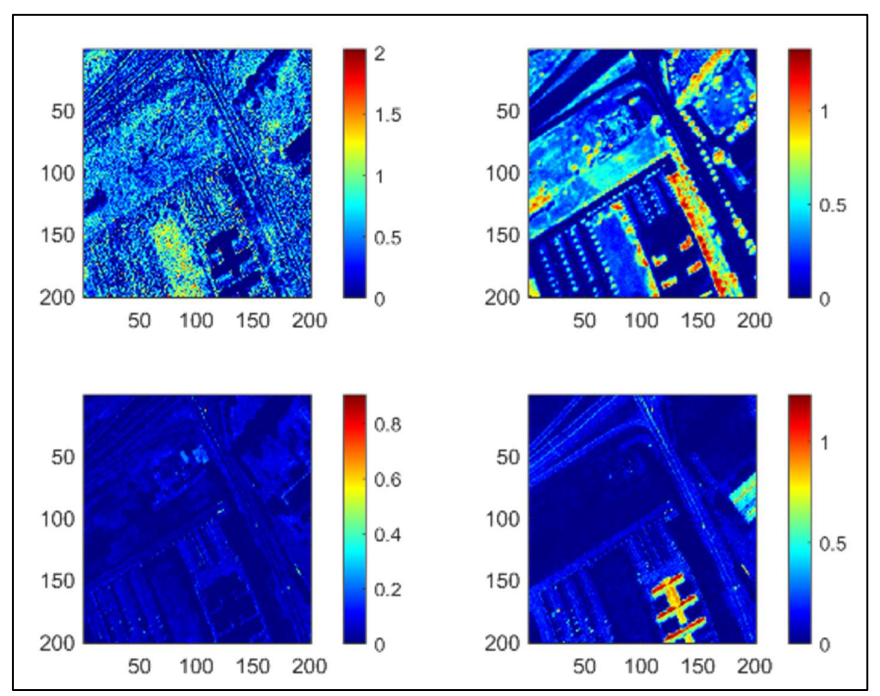


Figure 6-20. Abundances maps (Endmembers 1 to 4)

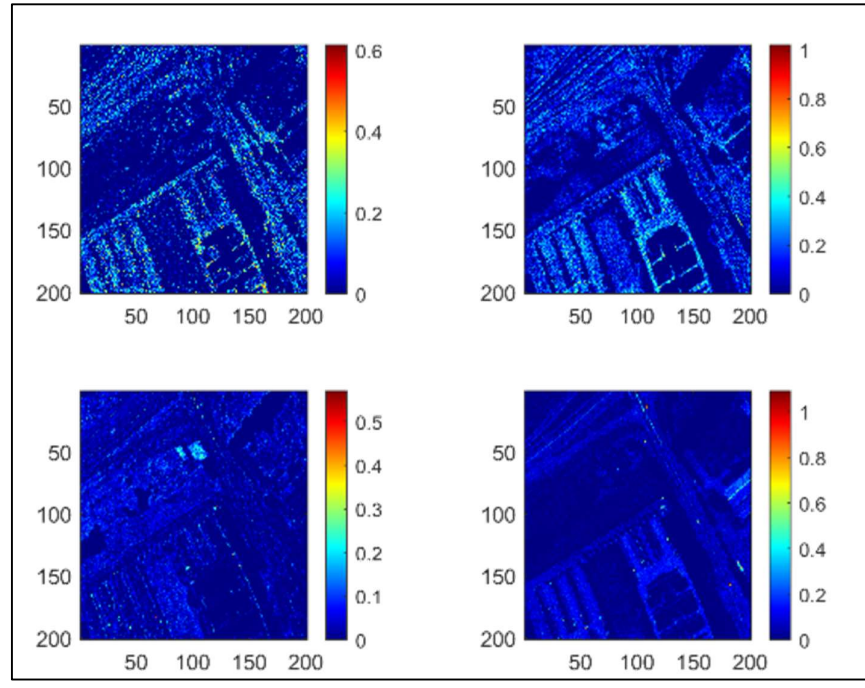


Figure 6-21. Abundances maps (Endmembers 5 to 8)

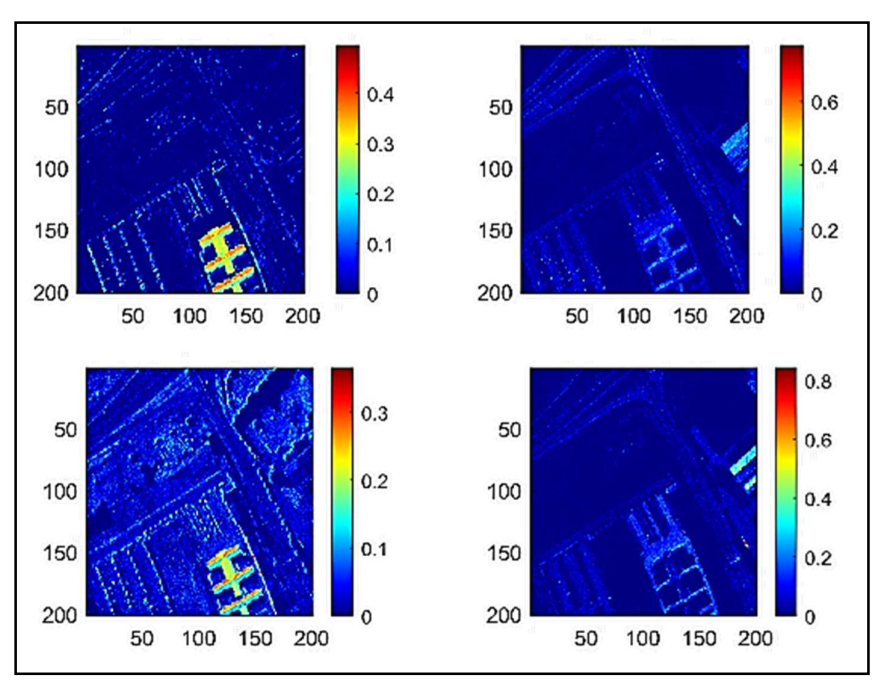
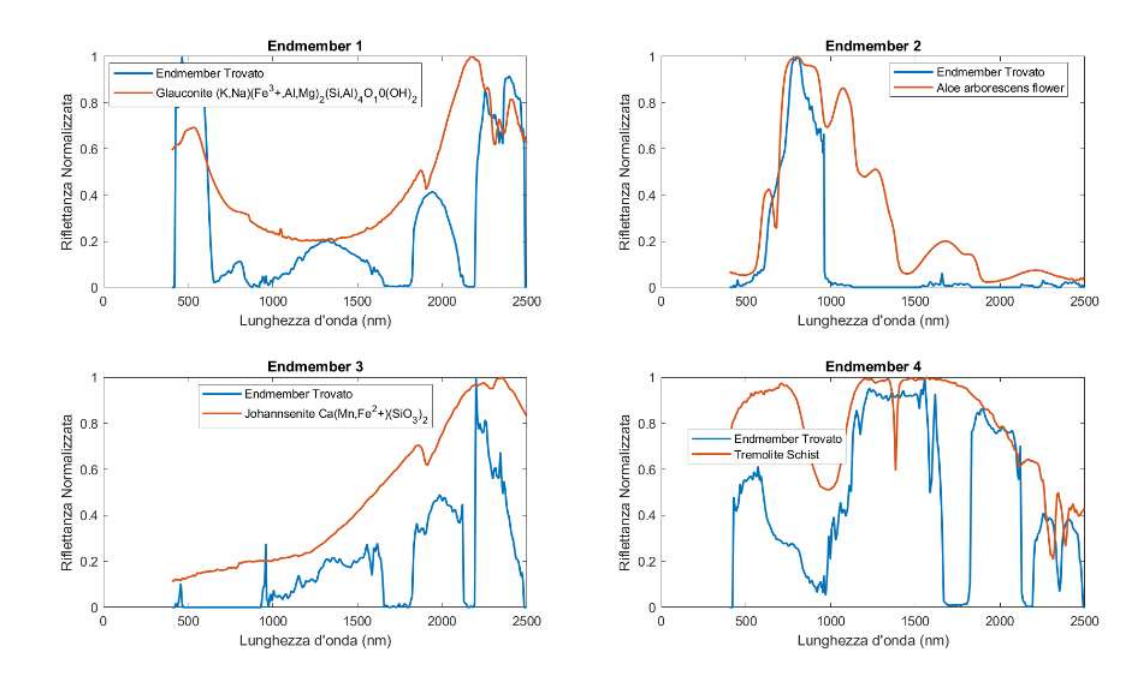
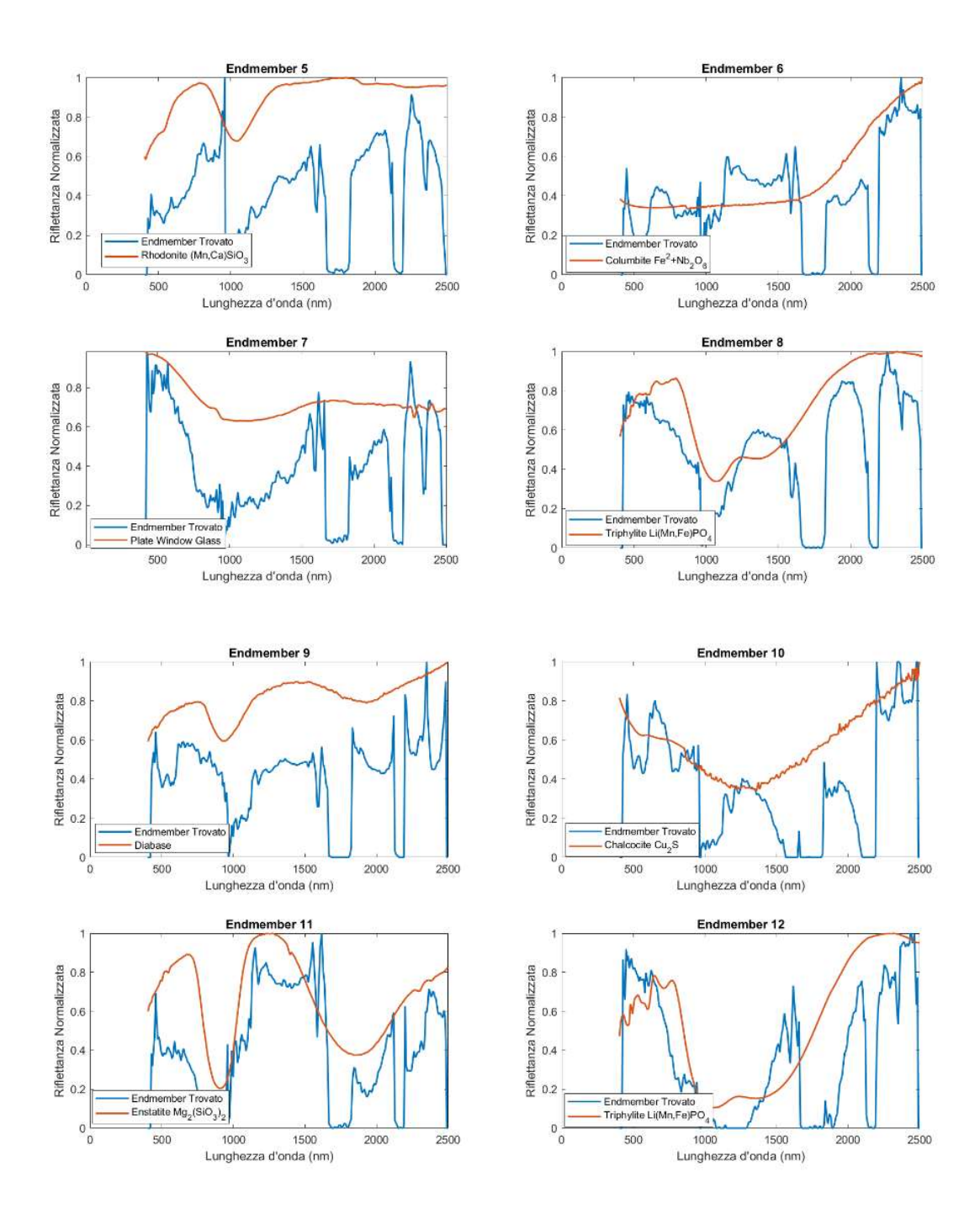


Figure 6-22. Abundances maps (Endmembers 9 to 12)

6.4 Association with existing library

The last part of the code aims to associate the extracted spectral signatures with the existing materials library from JPL. Even if the code extracts and plots the signatures for the associated endmembers, according to the criteria described in paragraph 5.5, it seems quite evident that the current association technique does not provide the adequate accuracy and confidence.





Chapter 7 Conclusions and Future Work

7.1 Summary and Contributions

This thesis presented a hybrid methodology for hyperspectral unmixing applied to data acquired by the Italian Space Agency's PRISMA satellite. The primary objective was to effectively decompose mixed pixels into constituent endmember spectra and their corresponding fractional abundances, leveraging both established geometric/statistical initialization techniques and advanced deep learning methods.

The proposed workflow commenced with data preprocessing and band-wavelength association specific to PRISMA data. Endmember initialization was performed using a combination of Vertex Component Analysis (VCA), Principal Component Analysis (PCA), and N-FINDR to provide robust starting points for subsequent refinement. A Convolutional Neural Network (CNN) was then employed to further extract and refine these endmembers, utilizing its capability to learn complex spectral features. Abundance maps were subsequently estimated using the non-negative least squares (Isqnonneg) algorithm, ensuring physically meaningful results. Finally, an attempt was made to associate the extracted endmembers with known material spectra from the NASA Jet Propulsion Laboratory (JPL) spectral library using Spectral Angle Mapper (SAM) and Spectral Information Divergence (SID) metrics.

The methodology successfully extracted distinct endmembers from the PRISMA dataset, as evidenced by the spectral signature plots and cross-correlation analysis. The corresponding abundance maps visually confirmed the spatial distribution of these endmembers, associating them with various ground features. Furthermore, the model's robustness was validated using the well-known Pavia University hyperspectral dataset, demonstrating its capability to effectively separate different land cover classes even without specific wavelength information for that sensor.

7.2 Advantages of the Proposed Method

The implemented spectral unmixing pipeline offers several advantages:

- 1. **Robust Initialization:** Utilizing multiple established techniques (VCA, PCA, N-FINDR) for endmember initialization provides a more robust starting point for the CNN, potentially reducing sensitivity to the limitations of any single method;
- 2. **Hybrid Approach:** Combining traditional unsupervised methods with a deep learning (CNN) approach leverages the geometric interpretability of the former and the feature extraction power of the latter, potentially leading to more accurate endmember identification than either approach alone;
- 3. **Computational Efficiency:** By operating on selected subsets of the hyperspectral data, the computational load is significantly reduced, enabling analysis on standard computing hardware within a reasonable timeframe.
- 4. **Demonstrated Generalizability:** Validation on the Pavia University dataset suggests that the core unmixing logic (initialization + CNN refinement) is adaptable to different hyperspectral sensors and scenes, enhancing its potential utility.

7.3 Challenges and Future Directions for Library Association

While the core unmixing process demonstrated promising results, the final step of associating extracted endmembers with the JPL spectral library revealed limitations in accuracy using the current SAM and SID implementation. Achieving reliable and accurate matching between sensor-derived endmembers and library spectra remains a significant challenge due to factors like atmospheric interference, sensor noise, spectral variability within materials, and differences between laboratory measurements and real-world conditions.

To enhance the accuracy of this association, several future research directions and hypotheses can be explored:

Advanced Similarity Metrics: Move beyond SAM and SID. Explore metrics that are
more sensitive to spectral shape and absorption feature characteristics, such as
correlation coefficients, spectral derivative analysis, or metrics based on continuum
removal;

2. Library Optimization:

- Contextual Filtering: Pre-filter the extensive JPL library based on the geographic context or expected land cover types within the PRISMA scene to reduce the search space and minimize spurious matches;
- Spectral Resampling: Investigate more sophisticated methods for resampling library spectra to match PRISMA's specific band wavelengths and spectral response functions, potentially going beyond the spline interpolation currently used;

- 3. **Feature-Based Matching:** Instead of comparing entire spectra, focus on extracting key spectral features (e.g., position, depth, width of absorption features) from both the extracted endmembers and library spectra and perform matching in this feature space;
- 4. **Machine Learning for Association:** Train a dedicated classification model (e.g., Support Vector Machine, tailored Neural Network) to map extracted endmember spectra to the most likely material class in the JPL library, potentially learning more complex relationships than simple distance metrics;
- 5. **Incorporating Spatial Context:** Utilize the generated abundance maps. High confidence in a match could be assigned if an endmember consistently maps to spatial features expected to consist of a certain material (e.g., a water-like endmember predominantly appearing over water bodies);
- 6. Addressing Spectral Variability: The JPL library typically contains representative single spectra. Develop methods to account for natural variability within material classes, perhaps by comparing extracted endmembers to statistical representations (mean, variance) of multiple library spectra for the same material or using spectral mixture analysis techniques within the library itself.

7.4 Concluding Remarks

This research successfully developed and validated a hybrid spectral unmixing workflow combining traditional initialization methods with a Convolutional Neural Network, demonstrating its effectiveness on PRISMA hyperspectral data. The approach benefits from robust initialization and the feature learning capabilities of CNNs while maintaining reasonable computational efficiency. While the core unmixing performed well, accurately associating the derived endmembers with standard spectral libraries remains an area requiring further investigation. The suggested future work, focusing on advanced similarity metrics, library optimization, improved atmospheric correction, and potentially machine learning-based association, offers promising avenues for significantly enhancing the reliability of material identification, thereby increasing the practical value of hyperspectral unmixing results derived from PRISMA and similar sensors.

Acronyms

AE Autoencoder

ASI Italian Space Agency

AVIRIS Airborne Visible/Infrared Imaging Spectrometer

BOA Bottom Of Atmosphere

CNN Convolutional Neural Network

CNM National Multimission Centre (Centro Nazionale Multimissione)

CO₂ Carbon Dioxide

E Endmembers (Mathematical notation)

EM Electromagnetic

EMR Electromagnetic Radiation

EO-1 Earth Observing-1 (NASA Satellite)

ESA European Space Agency

FDS Flight Dynamics System

FPA Focal Plane Array

GCP Ground Control Points

GIC Computational Intelligence Group (Group De Inteligencia Computacional)

GS Ground Segment

GSD Ground Sample Distance

HDF5 Hierarchical Data Format 5

H₂O Water Vapor

HSI Hyperspectral Imaging

HyPSEO Hyperspectral Precursor of the Sentinels for Earth Observation

ICU In-flight Calibration Unit

IDHS Image Data Handling Segment/Center

IR Infrared

JHM Joint Hyperspectral Mission

JPL Jet Propulsion Laboratory

KDP Key Data Parameters

L0 Level 0 (Data Processing Level)

L1 Level 1 (Data Processing Level)

L2B Level 2B (Data Processing Level)

L2C Level 2C (Data Processing Level)

L2D Level 2D (Data Processing Level)

LED Light Emitting Diode

LMM Linear Mixing Model

MCC Mission Control Center

ME Main Electronics

MPS Mission Planning System

MSE Mean Squared Error

N-FINDR Endmember extraction algorithm based on simplex volume maximization

NIR Near-Infrared

NMM Nonlinear Mixing Model

nm nanometers

OBDH On Board Data Handling

O₂ Oxygen

Ozone

OH Optical Head

PAN Panchromatic

PCA Principal Component Analysis

PDHT Payload Data Handling and Transmission

PPI Pixel Purity Index

PRISMA Hyperspectral Precursor of the Environmental Monitoring System (PRecursore IperSpettrale della Sistema di Monitoraggio Ambientale)

ReLU Rectified Linear Unit

ROSIS Reflective Optics System Imaging Spectrometer

SAM Spectral Angle Mapper

SCC Satellite Control Center

SCS Satellite Control System

SID Spectral Information Divergence

SI International System of Units (Sistema Internazionale)

SNR Signal-to-Noise Ratio

SVM Support Vector Machine

SWIR Short Wave Infrared

TMA Three-Mirror Anastigmat

TOA Top Of Atmosphere

TT&C Telemetry, Tracking, and Command

UTM Universal Transverse Mercator

UV Ultraviolet

VCA Vertex Component Analysis

VEGA European Advanced Generation Carrier Rocket (Vettore Europeo di

Generazione Avanzata)

VNIR Visible and Near Infrared

W Watts

Bibliography

- 1. Bioucas-Dias, J. M., Plaza, A., Camps-Valls, G., Scheunders, P., Nasrabadi, N. M., & Chanussot, J. (2013). Hyperspectral remote sensing data analysis and future challenges. IEEE Geoscience and Remote Sensing Magazine, 1(2), 6-36.
- 2. Boardman, J. W., Kruse, F. A., & Green, R. O. (1995). Mapping target signatures via partial unmixing of AVIRIS data. In Summaries of the Fifth JPL Airborne Earth Science Workshop (Vol. 1, pp. 23-26).
- 3. Nascimento, J. M., & Dias, J. M. (2005). Vertex component analysis: A fast algorithm to unmix hyperspectral data. IEEE Transactions on Geoscience and Remote Sensing, 43(4), 898-910.
- 4. Qian, Y., Jia, S., Zhou, J., & Robles-Kelly, A. (2011). Hyperspectral unmixing via sparsity-constrained nonnegative matrix factorization. IEEE Transactions on Geoscience and Remote Sensing, 49(11), 4282-4297.
- 5. Zhang, X., Sun, Y., Zhang, J., Wu, P., & Jiao, L. (2018). Hyperspectral unmixing via deep convolutional neural networks. IEEE Geoscience and Remote Sensing Letters, 15(11), 1755-1759.
- 6. Bioucas-Dias, J. M., Plaza, A., Dobigeon, N., Parente, M., Du, Q., Gader, P., & Chanussot, J. (2012). Hyperspectral unmixing overview: Geometrical, statistical, and sparse regression-based approaches. IEEE Journal of Selected Topics in Applied Earth Observations and Remote Sensing, 5(2), 354-379.
- 7. Plaza, A., Benediktsson, J. A., Boardman, J. W., Brazile, J., Bruzzone, L., Camps-Valls, G., ... & Thenkabail, P. S. (2009). Recent advances in techniques for hyperspectral image processing. Remote Sensing of Environment, 113, S110-S122.
- 8. Yokoya, N., Grohnfeldt, C., & Chanussot, J. (2017). Hyperspectral and multispectral data fusion: A comparative review of the recent literature. IEEE Geoscience and Remote Sensing Magazine, 5(2), 29-56.